NTNU

Norwegian University of
Science and Technology

Hydrodynamic Modelling Effects on Fatigue Calculations for Monopile Offshore Wind Turbines

Mohibb Ghani Malik

Marine Technology
Submission date: June 2016
Supervisor: Zhen Gao, IMT
Co-supervisor: Erin Bachynski, IMT

Norwegian University of Science and Technology
Department of Marine Technology

NTNU – Trondheim
Norwegian University of
Science and Technology

Hydrodynamic Modeling Effects on Fatigue Calculations for Monopile Offshore Wind Turbines

Mohibb Ghani Malik

June 2016

MASTER THESIS

Department of Marine Technology

Norwegian University of Science and Technology

Supervisor: Erin Bachynski

Co-Supervisor: Professor Zhen Gao

Preface

In order to complete the degree of Master of Science within the Department of Marine Technology at the Norwegian University of Science and Technology (NTNU), this Master Thesis has been written during the spring semester of 2016.

I would like to take this opportunity to thank my supervisor, Associate Professor Erin Bachynski. I have been given excellent advice and guidance during the process of writing the thesis, and this work would not have been possible without her.

I would also like to thank my friends and my fellow students at NTNU, for countless interesting discussions, and for providing motivation throughout the studies.

Trondheim, June 17, 2016

Mohibb Ghani Malik

Summary and Conclusions

For shallow and intermediate water depths, monopile foundations are the most commonly used concept, and is considered the most promising with respect to the cost of energy. The typical highest structural eigenperiods of these structures are usually between 3-5 seconds, and often coincide with the wave frequencies. Estimates of the fatigue life is therefore very dependent on accurate hydrodynamic modeling of the wave forces. In these cases, the waves are often relatively short compared to the structure, and the often used Morison's Equation is no longer accurate, as it does not account for diffraction.

In this thesis, a comparison between the standard Morison's equation and MacCamy-Fuchs diffraction theory has been performed. The responses and fatigue life of a 5 MW wind turbine was investigated, using both hydrodynamic theories.

The analyses showed that the wind turbine experienced small differences as a result of the hydrodynamic modeling. Since wave diffraction affects small waves, the results were different at different depths. At the mean sea level, MacCamy-Fuchs resulted in approximately 3% lower fatigue damage. However, at the bottom, where only the large waves affect the structure, MacCamy-Fuchs resulted in approximately 3 % higher fatige. This suggests that the wind turbine in question is not very sensitive to diffraction.

It was however seen that the fatigue damage was dominated by load cases with large aerodynamic thrust, suggesting that the structure is more sensitive to aerodynamic loads than hydrodynamic loads, as should be expected from a monopile structure at shallow water depth.

TABLE OF CONTENTS

LIST OF FIGURES

LIST OF TABLES

NOMENCLATURE

Abbreviations

ABAM Adams-Bashforth-Adams-Moulton predictor-corrector method

BEM Blade Element Momentum

CDF Cumulative Distribution Function

GDW Generalized Dynamic Wake

MLE Maximum Likelihood Estimation

MSL Mean Sea Level

NKUA National and Kapodistrian University of Athens

NTM Normal Turbulence Model

NWP Normal Wind Profile

OC3 Offshore Code Comparison Collaboration

PDF Probability Density Function

TSR Tip Speed Ratio

Symbols

C_D Drag Coefficient

C_I Inertia Coefficient

f_{1p}	Rotor Frequency
f_{3p}	Blade Passing Frequency
h	Water Depth
H_s	Significant Wave Height
k	Wave Number
T_p	Spectral Peak Period
U_w	Mean Wind Speed
Z	Placement Along Tower Height
φ	Placement around the Tower Circumference
θ	Misalignment between Wind and Waves
α_H	Shape Parameter of Weibull Distribution for Wave Height
β_H	Scale Parameter of Weibull Distribution for Wave Height
μ_T	Mean Value of Lognormal Distribution for Peak Period
σ_T	Variance vof Lognormal Distribution for Peak Period
α_U	Shape Parameter of Weibull Distribution for Wind Speed
β_U	Scale Parameter of Weibull Distribution for Wind Speed

1. INTRODUCTION

The wind industry has experienced a period of large growth the last decade. Countries are investing more money in the industry, and the year 2015 ended with new installations exceeding 63 MW globally. The record for global annual installed wind capacity has been broken every year since 2000 (except 2013), with China, USA and Germany leading the way (GWEC, 2015). The general trend in the industry is to move towards larger rotors, larger generators, and correspondingly larger support structures.

These large wind turbines have been met with a lot of resistance due to the aesthetics and the level of noise. One solution to this has been to move the wind turbines offshore, where the energy potential is also much greater than on land. The largest offshore wind turbines installed today range from 5-7 MW, and the sizes are expected to increase up to 10-20 MW in the coming years.

For shallow and intermediate water depths, large monopile foundations are considered to be the most promising with respect to the levelized cost of energy (LCOE). For this reason, monopile foundations are by far the dominant foundation for offshore wind turbines, and are expected to stay dominant for some time.

1.1 Motivation

Due to the higly complex dynamic loadings on a offshore wind turbine, resulting from aerodynamic and hydrodynamic loads, the fatigue of the structure is an important design factor. The highest structural eigenperiods of large monopile

structures are typically between 3-5 seconds, and often coincide with the wave frequencies. Estimates of the fatigue life is therefore very dependent on accurate hydrodynamic modeling of the wave forces. For large wind turbines, the waves may often be relatively short compared to the size of the structure. In these cases, the diffraction of the waves becomes important, and the often used Morison's Equation is no longer accurate, as it does not account for diffraction.

For the case of vertical cylinders, stretching from the bottom through the waterline, MacCamy-Fuchs theory may be used to calculate the forces on the cylinder. MacCamy-Fuchs theory may therefore be used to calculate the wave forces on a monopile offshore wind turbine, while accounting for the diffraction of the short waves.

In this thesis, an implementation of MacCamy-Fuchs theory has been developed for use with FAST, a simulation tool for offshore wind turbines. In order to investigate the hydrodynamic modeling effect on fatigue calculations, the responses have been compared to the standards Morison's Equation.

1.2 Limitations

The main limitations of the work in this thesis is in regard to the kinematic model for the wave zone. At the time of writing, kinematic stretching of the waves has not been implemented in FAST. For small waves, this does not affect the responses significantly, but for large waves, the loads on the structure is not realistic, as the whole wave crest disappears. However, as the main purpose of the thesis is to compare the two hydrodynamic modeling methods, this is not a problem.

In addition to the wave stretching, a limitation is the choice of site. As explained in Section 2.3, the depth of the site of the hindcast data is larger than the depth of the wind turbine. The effect of this could have been mitigated by taking into account the transformation of waves to shallow water, but this was

not done, as it is outside the scope of the thesis. It should still be noted that the site is representative of a shallow water site for a monopile wind turbine.

The fatigue damage results in Chapter 8 show very large damage. This is due to the fact that all wind is coming from the same direction. A limitation of the fatigue results is that the damage is unrealistically large. For a proper fatigue design, this has to be be taken into account by simulating the wind from different directions. However, the calculations are applicable for the comparisons performed in this thesis.

1.3 Structure of the Report

The main part of this thesis is structured as follows: Chapter 2 defines software used in this thesis, and describes the wind turbine and the site on which it is located. The dimensions of the wind turbine, as well as a brief description of its main behavior is discussed here. A review of the relevant theory for the thesis is then presented in Chapter 3, touching upon aspects such as aerodynamics, fatigue calculation and modal theory. The two main hydrodynamic models investigated in this thesis are also described in this chapter. In Chapter 4, a discussion is presented on how the long term environmental conditions have been analyzed, with the corresponding probability distributions. The approach used to apply the long term environmental conditions, and how to model the short term conditions is described in Chapter 5. It is here described how the wind and wave spectra have been modeled in this thesis. Chapter 6 then describes the load cases that have been used, to give an understanding of the loads experienced by the wind turbine. The post-processing of the results is discussed in Chapter 7. The methods used to investigate how the loads affect the fatigue life is discussed here, as well as the actual differences between the hydrodynamic models. This is followed by an investigation of the results in Chapter 8, where the effects of different weather conditions are discussed. An investigation is also performed on the fatigue life at different places on the structure, with respect to the hydrodynamic modeling methods. Lastly, the conclusions of the work is presented in Chapter 9, with respect to the objectives. Recommendations on further work are also given here.

2. SYSTEM DEFINITION

2.1 Software

The main software used for simulation of the wind turbine is FAST. FAST is a free, open source CAE tool developed by the National Renewable Energy Laboratory (NREL). It joins aerodynamics, hydrodynamics, structural dynamics and electrical/control systems into coupled time-domain simulations of horizontal axis wind turbines.

FAST combines modal (tower and blades) and multibody (nacelle, generator, platform) dynamics, and models conventional 3-bladed wind turbines with up to 24 degrees of freedom, including platform motions (not applicable for the bottom-fixed monopile substructure in this thesis), tower, nacelle and blade motions.

The wind data was generated using the NREL tool TurbSim, a stochastic, full-field simulator for turbulent wind.

2.2 Wind Turbine

2.2.1 Turbine Structure

In this thesis, all simulations have been performed on the 5 MW Baseline Wind Turbine (Figure 2.1) developed by Jonkman et al. (2009). The support structure under water is the monopile structure used in the Offshore Code Comparison Collaboration (OC3) studies (Jonkman and Musial, 2010). The wind turbine has a hub height of 90 m above the mean sea level (MSL), with a rotor diameter of 126 m. The foundation of the structure is a rigid connection to the bottom. It should be noted that this is a simplified way of modeling the substructure, but for the comparison purpose of this work, it is adequate.

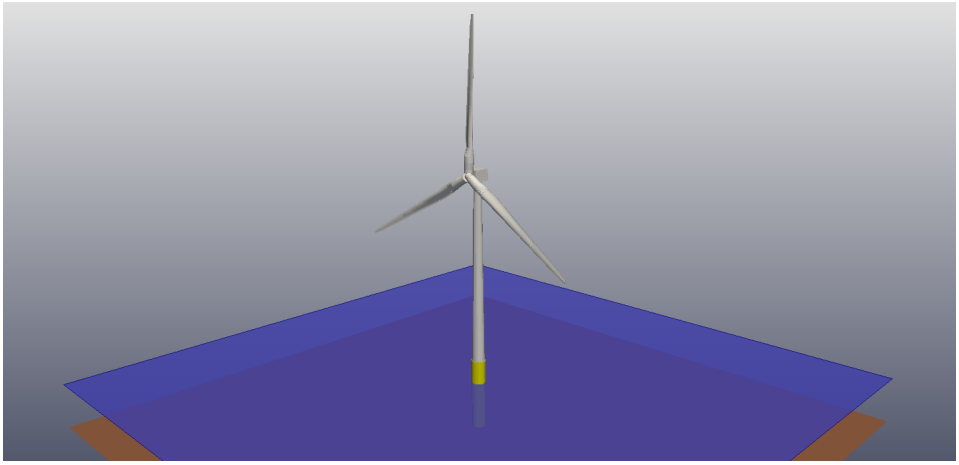

Fig. 2.1: FAST model of the NREL 5 MW Baseline Wind Turbine

The monopile support structure has a constant diameter (6 m) and thickness (60 mm), and stretches from the bottom to 10 m above MSL. The base of the tower has a diameter of 6 m and a thickness of 27 mm, and tapers linearly towards the top diameter (3.87 m) and thickness (19 mm). A summary of the properties of the wind turbine is shown in Table 2.1

Tab. 2.1: Summary of properties of the NREL 5MW baseline wind turbine (Adapted from Jonkman and Musial, 2010)

Rating Rotor orientation, configuration	Upwind, 3 blades
Control	Variable speed, collective pitch
Drivetrain	High speed, multiple-stage gearbox
Rotor, hub diameter	126 m, 3 m
Hub height	90 m
Water depth	20 m
Cut-in, rated, cut-out wind speed	3 m/s, 11.4 m/s, 25 m/s
Cut-in, rated rotor speed	6.9 rpm, 12.1 rpm
Rated tip speed	80 m/s
Overhang, shaft tilt, precone	5 m, 5°, 2.5°
Rotor mass	110,000 kg
Nacelle mass	240,000 kg
Tower mass	347,500 kg
Coordinate location of overall center of mass (CM)	(-0.2 m, 0.0 m, 64.0 m)

2.2.2 Control Systems

Like most industrial, large scale wind turbines made today, the NREL 5 MW reference wind turbine has a variable speed, variable pitch control system. For the NREL turbine, this means that the control system consists of a variable speed generator torque controller, and a collective blade pitch controller. The goal of the control system is to optimize the power output for wind speeds below rated wind speed (11.4 m/s), while limiting the loads on the turbine when the wind speeds are higher than rated. For wind speeds below rated, this is done by varying the speed of the rotor to maintain optimal tip speed ratio (TSR), the ratio between the incoming wind velocity and the tangential speed of the blade tips. For wind speeds above rated, the blades are pitched to maintain the rated power output from the generator.

The generator torque controller regulates the torque of the generator as a function of the filtered generator speed. The generator speed is filtered using recursive, single-pole, low-pass filter with exponential smoothing. Three distinct control regions are incorporated in the variable speed controller. Region 1

is for wind speeds below cut-in speed (3 m/s), where the torque is zero, and all the available energy is used to accelerate the rotor. In Region 2, the generator torque is changed to optimize the power output from the generator. In Region 3, above rated wind speed, the generator torque is regulated to keep the generator output constant at 5 MW. The control systems also incorporate transition regions, 1½ and 2½, to ease the transition between the regions.

Like the generator torque, the collective pitch is regulated by measuring the generator speed. The blades may pitch between 0° and 90°, with a pitch rate limit of 8°/sec. For low wind speeds, the pitch angle stays zero, while for wind speeds above rated, a PI-controller is incorporated to compute the pitch angle based on the error between the rated and the filtered generator speeds. The proportional and integral gains are based on the previous pitch angle. Figure 2.2 shows a flowchart of the control systems, with both the look-up table for the generator torque, and the PI controller for the collective blade pitch.

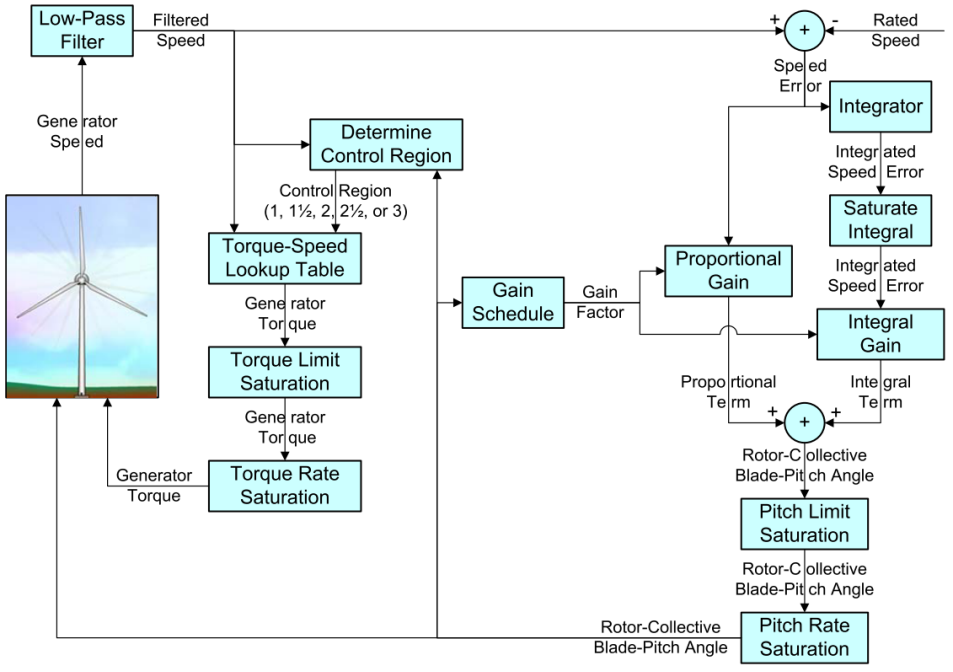

Fig. 2.2: Flowchart of the control systems (Jonkman et al., 2009)

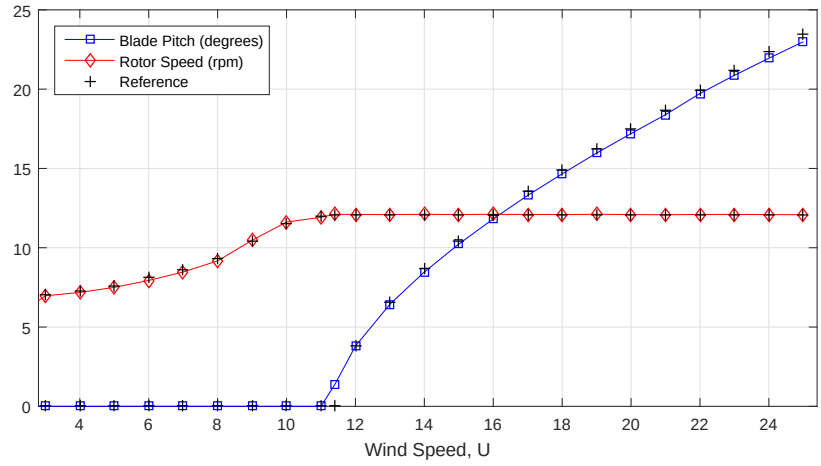

(a)

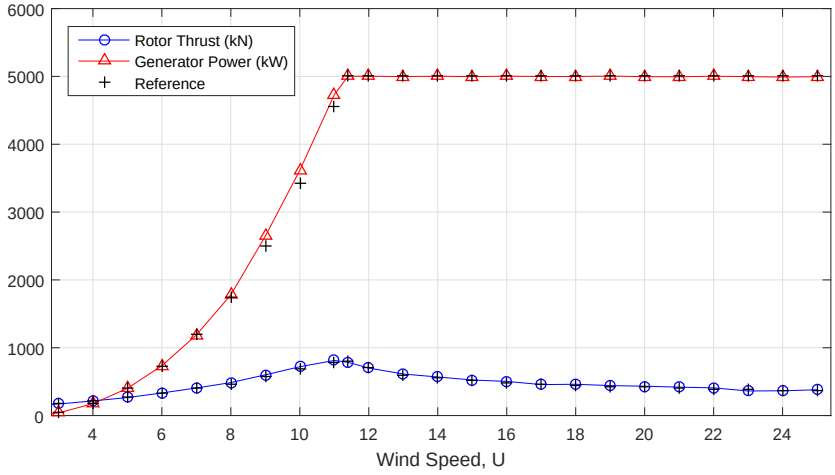

(b)

Fig. 2.3: Steady State Responses

When evaluating the steady state responses of the wind turbine, the different regions of the power curve may be seen. Figure 2.3 shows the steady state results for Blade Pitch, Rotor Speed, Rotor Thrust and Generator Power. The results were obtained by from FAST, by subjecting the wind turbine to constant and uniform winds, with speeds between the cut-in and cut-off speed. For verification, the obtained results are compared to the reference values calculated

by Jonkman et al. (2009). The small differences in Blade Pitch and Generator Power are due to the fact that the reference values are computed using an older version of FAST (FAST v7), which does not include torsional, shear, or extensional degrees of freedom for the blades.

2.2.3 Natural Frequencies

When considering the dynamic responses of a wind turbine, a consideration of the natural frequencies is very important. If the excitation frequencies are at or close to any of the eigenfrequencies, the loads may become very large. This may affect both the maximum loads as well as the fatigue life.

The natural frequencies of the structure in this thesis were calculated in the OC3 studies (Jonkman and Musial, 2010), and are shown in 2.4. The natural frequencies are compared to the ranges of peak wave frequencies (defined in Chapter 6), and the rotor and blade frequencies, f_{1p} and f_{3p} (defined in Section 3.2).

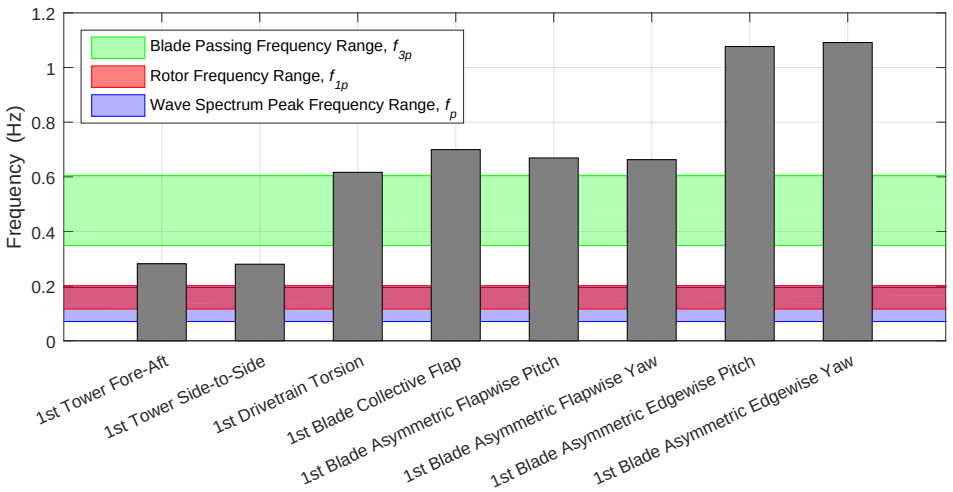

Fig. 2.4: Eigenfrequencies of the system, compared to excitation frequency ranges

2.2.4 Coordinate System

The coordinate system utilized in this thesis is the same as in FAST. This means that the x-axis points in the downwind direction, while the the y-axis points to the left when looking downwind and the z-axis points vertically upwards. The origin of this inertial frame coordinate system is at the intersection between the centerline of the tower and the connection between the tower and substructure. For the monopile used in this thesis, the origin is therefore located at the mean sea level. Figure 2.5 shows the main coordinate system as described. Note that the figure shows a downwind turbine, whereas the actual turbine used in this thesis is an upwind turbine.

Fig. 2.5: Main coordinate system used in FAST, shown on a downwind turbine (Jonkman and Buhl, 2005)

2.3 Site

As the NREL 5 MW Baseline Wind Turbine is a reference wind turbine, it is not designed for a specific site. It is, however, designed for a theoretical site with water depth of 20 m. The environmental raw data used in this thesis are therefore generated by a numerical hindcast model, provided by the National and Kapodistrian University of Athens (NKUA) MARINA WP2.

Site 15 from Li et al. (2013) was chosen, as it has characteristics that may be applied for the purpose of this thesis. The location, indicated in Figure 2.6, has a larger depth than the turbine site. For the purposes of this thesis, the difference was not considered, and the raw data were analyzed to decide upon the environmental conditions. This is explained further in Chapters 4 and 6.

Tab. 2.2: General information about the selected site (adapted from Li et al. (2013))

Area	North Sea
Name	Denmark, North Sea Center
Water Depth	29 m
Distance to shore	300 km
Coordinates	55.13N, 3.43E

Fig. 2.6: Location of the selected site (Li et al., 2013)

3. BACKGROUND THEORY

The following chapter presents the relevant theory needed to give a good understanding of underlying problem, the results and the following discussion.

3.1 Hydrodynamic Modeling

The hydrodynamic loads used in this thesis are modeled using two different theories; Morison's Equation and MacCamy-Fuchs Diffraction Theory. Both theories are explained briefly in Sections 3.1.1 and 3.1.2, and examined further in Malik (2015).

3.1.1 Morison Equation

The empirical Morison equation, Equation (3.1), is the most widely used formulation for calculating wave forces on cylinders. The force on a disk of the cylinder (with thickness $\mathrm{d}z$) is calculated from the wave kinematics of the undisturbed, long crested waves.

$$\mathrm{d}F_{M1} = \mathrm{d}F_D + \mathrm{d}F_I \tag{3.1a}$$

$$\mathrm{d}F_D = \frac{1}{2} C_D \rho D u|u| \mathrm{d}z \tag{3.1b}$$

$$\mathrm{d}F_I = C_M \rho \frac{\pi D^2}{4} \frac{\partial u}{\partial t} \mathrm{d}z \tag{3.1c}$$

Morison's equation consists of two terms, a drag term and an inertia term. The drag force, $\mathrm{d}F_D$, is calculated from the drag coefficient, C_D, cylinder diame-

ter, D, water density, ρ, and the particle velocity at the center of the cylinder, u, while the inertia force is related to the acceleration of the water particle, $\frac{\partial u}{\partial t}$ and the inertia coefficient, C_M. Both C_D and C_M vary depending on many different parameters, such as the Reynolds number, the Keulegan–Carpenter number or the surface roughness. For simplicity, a single value is often used over the whole frequency spectrum.

Utilizing linear wave theory, the total force on the cylinder is calculated by integrating the force along the length of the cylinder. As this is purely linear, the wave kinematics are only integrated to mean sea level, not to the wave crest. This is discussed in briefly in Section 3.1.3.

$$F_{M1} = \int_{-h}^{0} \mathrm{d}F_{M1} = \int_{-h}^{0} \mathrm{d}F_D + \int_{-h}^{0} \mathrm{d}F_I \tag{3.2}$$

It should be noted that Morison's equation assumes the long wave approximation, meaning that the size of the cylinder is small compared to the wave length, and that the cylinder does not affect the wave. When the size of the cylinder is comparable to the wave length $\left(\frac{\lambda}{D} \lesssim 5\right)$, Morison's equation is less accurate, as diffraction becomes more important.

3.1.2 MacCamy-Fuchs Diffraction Theory

Given a vertical cylinder that extends from the seabed and through the waterline, the wave forces may be calculated using the work of MacCamy and Fuchs (1954). They formulated an analytical approach for calculating the wave loads on cylinders, that in turn can be used to formulate an equivalent inertia coefficient for all values of $\frac{\lambda}{D}$. By utilizing the velocity potential of the incident wave, along with linear wave theory, MacCamy and Fuchs showed that the force on

the differential cylinder segment may be written as:

$$\mathrm{d}F_{MF} = \frac{2\rho g H}{k} \frac{\cosh\left(k\left(h+z\right)\right)}{\cosh\left(kh\right)} A(kr) \cos\left(\omega t - \alpha(kr)\right) \tag{3.3}$$

where

$$A(kr) = \frac{1}{\sqrt{\left(J_1'(kr)\right)^2 + \left(Y_1'(kr)\right)^2}} \tag{3.4}$$

$$\alpha(kr) = \arctan\left(\frac{J_1'(kr)}{Y_1'(kr)}\right) \tag{3.5}$$

Here, J_1' and Y_1' represent the differentiated Bessel functions of the first and second kind, respectively. H represents the wave height, h is the total depth, z is the vertical position, k is the wave number, ω is the wave frequency, and r is the radius of the cylinder.

The total force on the cylinder, found by integrating over the length of the cylinder, was shown to be:

$$F_{MF} = \int_{-h}^{0} \mathrm{d}F_{MF} = \frac{2\rho H\, A(kr)}{k^2} \frac{\omega^2}{k} \cos(\alpha)\cos(\omega t) + Q\sin(\omega t) \tag{3.6}$$

By comparing Equation (3.6) to Morison's equation, an equivalent inertia coefficient may be found:

$$C_M^{eq.} = \frac{4A(kr)}{\pi^3} \left(\frac{\lambda}{D}\right)^2 \cos(\alpha) \tag{3.7}$$

As Figure 3.1 shows, diffraction becomes important for $\frac{\lambda}{D} \lesssim 5$. This is also seen when comparing the equivalent inertia coefficient to the constant value for Morison's equation in Figure 3.2. A constant value of $C_M = 2$ is approximately equal to the analytical value of MacCamy-Fuchs for long waves ($\frac{\lambda}{D} \gtrsim 5$). For shorter waves, the constant value will significantly overestimate the forces. The

effect of this is investigated in Malik (2015), and later in this thesis.

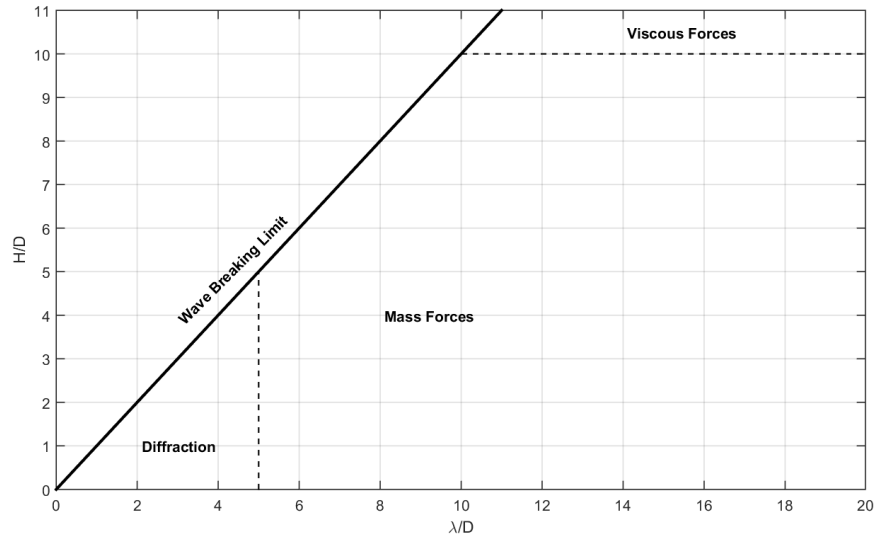

Fig. 3.1: Relative importance of mass, viscous drag and diffraction forces on marine structures [Adapted from Faltinsen (1990)]

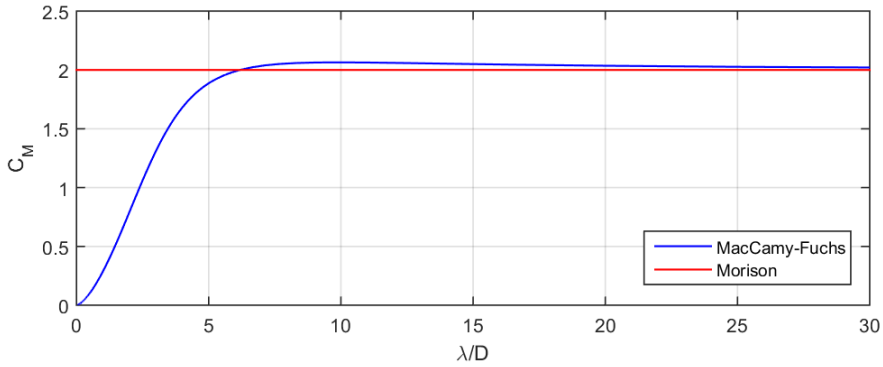

Fig. 3.2: Inertia Coefficients, C_M (Malik, 2015)

3.1.3 *Wave Stretching*

When working with linear wave theory, the wave kinematics are not calculated above the mean sea level. There are several methods of estimating the kinematics between MSL and the wave crest for linear waves, such as vertical extrapola-

tion or Wheeler stretching.

With Vertical extrapolation, the wave kinematics above MSL are assumed equal to the kinematics at MSL, while with Wheeler stretching, the wave kinematics are calculated up to the MSL, and then stretched to fit to the true surface elevation, by:

$$z' = \frac{h(h+z)}{h-\eta} - h; \tag{3.8}$$

where η is the instantaneous wave elevation.

However, as wave stretching has not yet been implemented in the current version of FAST (v8.12.00a-bjj, 6-Oct-2015), it has not been applied in this thesis. The wave kinematics above MSL are therefore assumed equal to 0, while the kinematics below MSL are calculated using linear wave theory. A comparison of the different methods is shown in Figure 3.3.

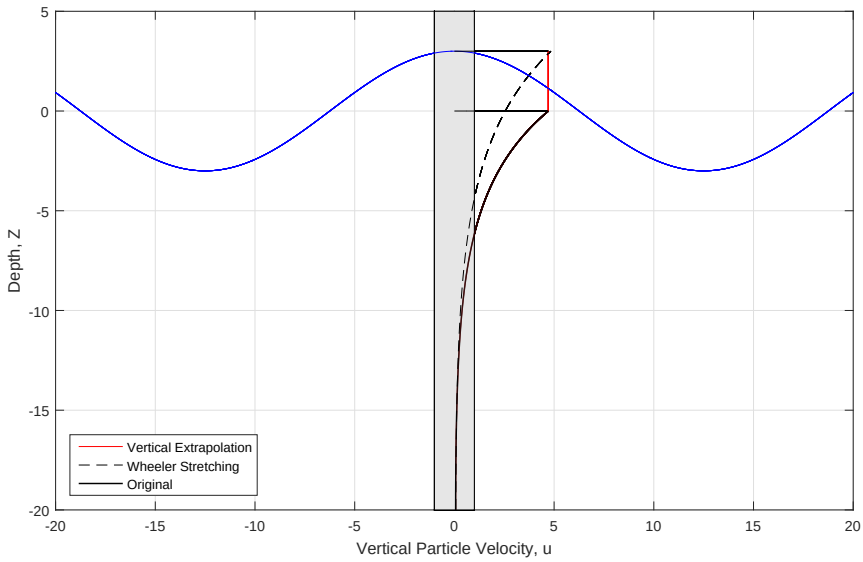

Fig. 3.3: Comparison of wave stretching models

3.2 Aerodynamic Modeling

The aerodynamic loads from the wind on the blades may be modeled using different approaches. The applied models in FAST/AeroDyn are called Blade Element Momentum (BEM) and Generalized Dynamic Wake (GDW). Both of these models are explained briefly in the following sections, along with their respective advantages and drawbacks. A more detailed description may be found in the AeroDyn manual (Moriarty and Hansen, 2005).

3.2.1 Blade Element Momentum Theory

Blade Element Momentum theory is one of the most commonly used theories used to calculate aerodynamic loads on rotor blades, and is a combination of Blade Element theory and Momentum theory (actuator disk theory).

Using Blade Element theory, the blades are divided into small 2-dimensional foil elements. The inflow velocities and angles are computed, along the local aerodynamic forces for each element. To find the total forces on the turbine, all

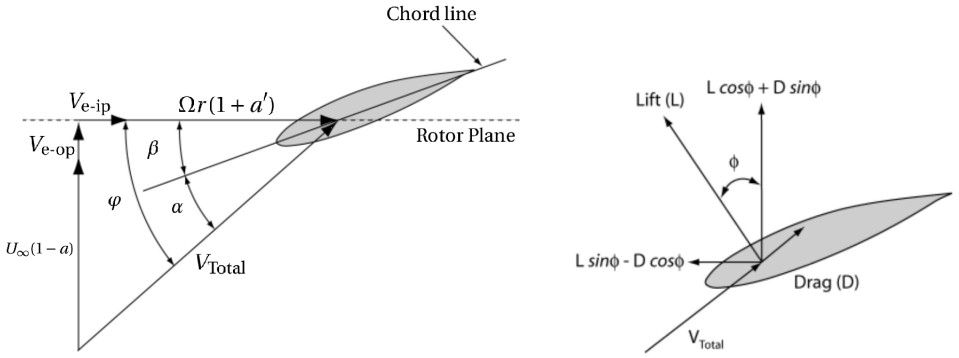

Fig. 3.4: Local inflow angles, velocities and forces (Moriarty and Hansen, 2005)

the local element forces are integrated along the length of the blade.

When the blade elements rotate around in the rotor plane, they trace out annular regions of the plane, as shown in Figure 3.5. Momentum balance is ap-

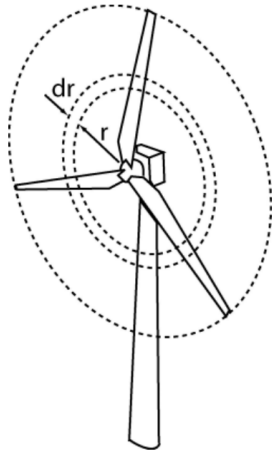

Fig. 3.5: Annular plane used in blade element momentum theory (Moriarty and Hansen, 2005)

plied across these annular regions, and the induced wind velocities may be calculated from the momentum lost in the axial and tangential directions. These induced velocities affect the inflow velocities, which in turn affects the forces on the blades. The aerodynamic forces and the local velocities are then found by iteration.

When using BEM theory, the procedure can be considered to be quasi-static. This means that following a change of rotor speed, blade pitch angle or wind velocity, the induced velocities change instantaneously. This is not the case for a real wind turbine, as it takes some time for the flow to react to the changes.

One limitation of BEM theory is that the blades are assumed to be in the rotor plane. This means that the theory breaks down, and lead to large errors when the deflections are large. Another limitation is that the blades are assumed to be 2-dimensional, meaning that flow along the blade span is neglected. BEM theory is therefore less accurate for heavily loaded rotors, where the spanwise flow may be large.

When using BEM theory in FAST, the span wise flow is accounted for by applying different correction factors, such as the Prantdl tip loss correction (flow

across the tip) and the Glauert correction (large induction factors).

3.2.2 Generalized Dynamic Wake

An alternative method to calculate the induced velocities and the aerodynamic forces is the Generalized Dynamic Wake (GDW) method, a method originally developed for helicopters. Generalized Dynamic Wake is based on an acceleration potential solution of Laplace's equation, and is appropriate for lightly loaded rotors. For the NREL 5MW Wind Turbine, with the operational profile described in Section 2.2.2, this means that GDW is only appropriate for wind speeds above 8 m/s.

An advantage of GDW is that it inherently includes some of the effects that are neglected in BEM, such as dynamic wake and tip loss. Another advantage is that the solutions are calculated from a set of differential equations, meaning iterations are not required. It should also be noted that using GDW theory will lead to slightly more damping. This may be shown by looking at the stress at the bottom of the monopile. Figure 3.6 show the stress at the bottom for wind speeds just above the limit for GDW (9 m/s) and for just above rated wind speed (12 m/s). The time series show that BEM generally results in slightly larger amplitudes. This is also seen in the power spectra in Figure 3.7, where BEM results in more energy over the spectrum, as a result of less damping.

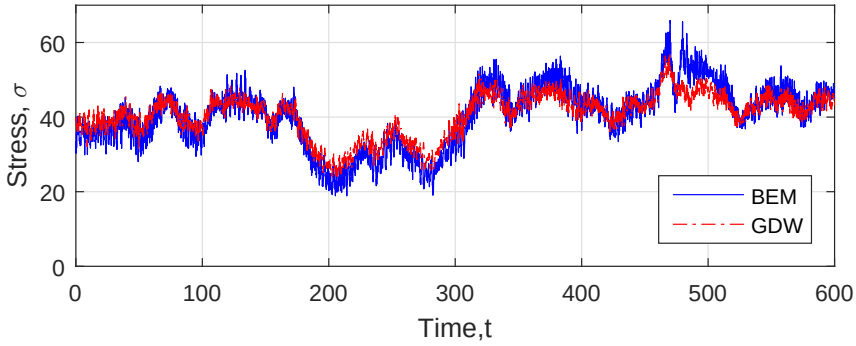

(a) $U_w = 9m/s$

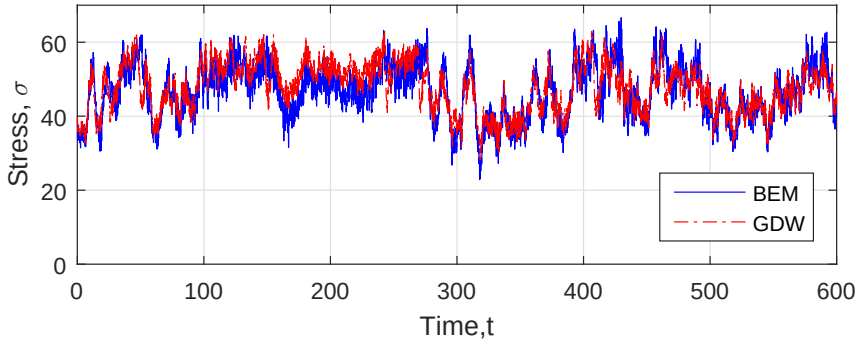

(b) $U_w = 12m/s$

Fig. 3.6: Time series of the stress at the bottom - BEM vs GDW

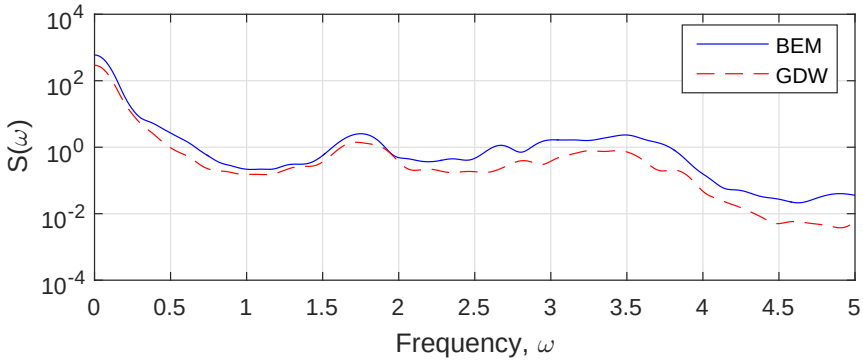

(a) $U_w = 9m/s$

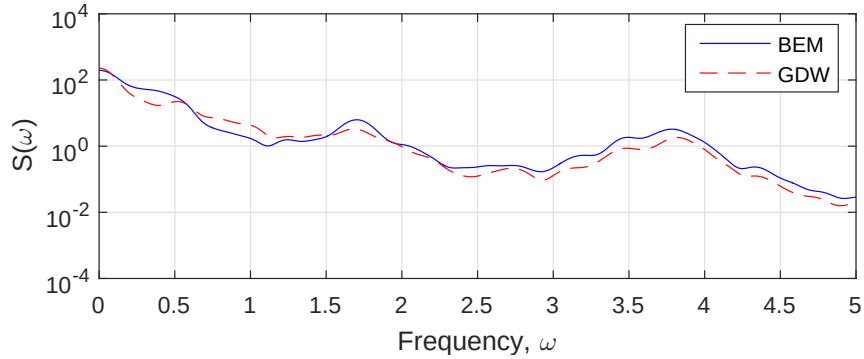

(b) $U_w = 12m/s$

Fig. 3.7: Power spectra of the stress at the bottom - BEM vs GDW

3.2.3 Tower Shadow Effects

When the wind hits the tower, it is disturbed by the presence of tower. As the wind must travel around the tower, the local inflow is changed. This means that the wind speeds are affected both in front of, and behind the tower. The modeling of this tower shadow effect in AeroDyn is based on a potential flow solution around a cylinder. Figure 3.8 shows an example of the velocity deficit as a result of the tower shadow, compared to the rotor radius, R, and the tower diameter, D.

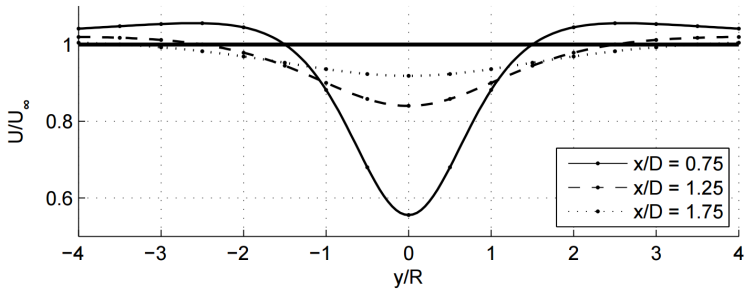

Fig. 3.8: Tower Shadow Effect

As the figure shows, the wind speed in front of the tower is reduced significantly, meaning that whenever a blade passes through this zone, it will experience slightly lower wind speeds. The tower shadow, along with the wind shear, gives rise to noticeable fluctuations in the responses. Wind shear refers to the variation of wind with height, as described by the power law in Equation 5.4 in Section 5.1. The fluctuations are related to the rotor frequency, f_{1p}, and the blade passing frequency, $f_{3p} = 3\ f_{1p}$ (for a three bladed turbine). These can often be seen as peaks in the power spectra, and must be considered when analyzing fatigue life.

3.3 Fatigue Calculation

Cyclic loading on a structure will in many cases lead to crack growth/propagation and damage in the structure. Even when the loads are lower than the yield stress, the sheer number of load cycles over the lifetime may lead to failure. For this reason, it is important to consider the fatigue damage when designing offshore wind turbines.

3.3.1 SN-Curves

When calculating the fatigue damage, the mean value of the stress is less important than the actual deviation. For constant amplitude loading (sinusoidal load history), the number of cycles to failure, N, is calculated using SN-curves, which relate the stress amplitude, $\Delta\sigma$, to N (see Figure 3.9). The SN-curves are obtained from material testing, by subjecting samples to different cyclic loadings until failure.

The SN-curves in DNV-RP-C203 (2011) are defined by Equation (3.9):

$$\log N = \log \bar{a} - m \log\left(\Delta\sigma \left(\frac{t}{t_{ref}}\right)^k\right) \tag{3.9}$$

. The parameters $\bar{a}$, m, k and t_{ref} depend largely on the weld geometry and the environment. The type and quality of welds may introduce stress concentrations, which will affect the fatigue life. Similarly, the presence of corrosive environment also reduces the fatigue life.

3.3.2 Cumulative Damage

As mentioned above, SN-curves apply to constant amplitude load histories. For load histories with variable amplitude, the time history is broken down into individual cycles, and then summed up to get a distribution of stress ranges. Tech-

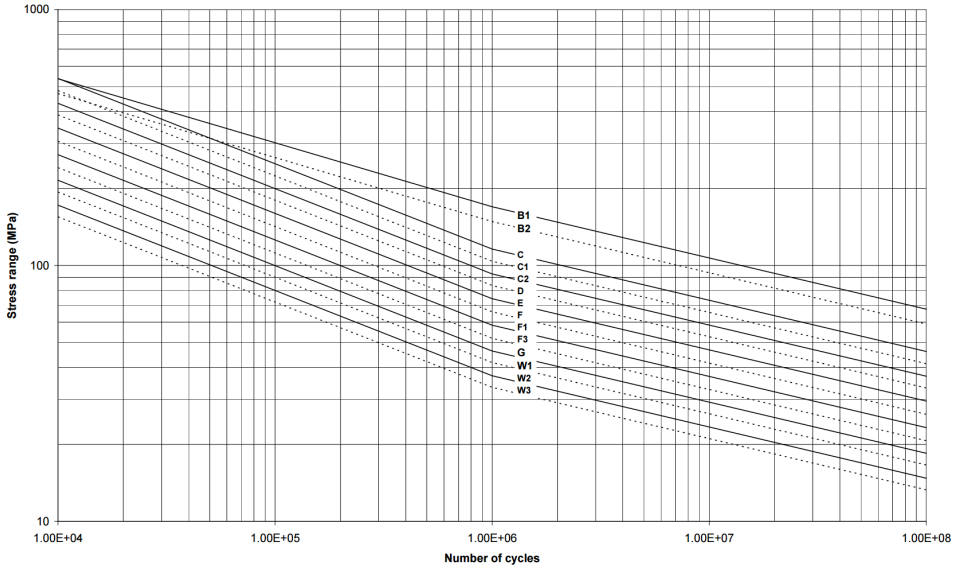

Fig. 3.9: S-N curves in seawater with cathodic protection, (DNV-RP-C203, 2011)

niques such as rainflow counting are applied to count the number of cycles in each stress range. The rainflow counting method has gotten its name from the analogy of rain water falling down a pagoda roof, and follows the rules below (Berge, 2006):

1. Rain flows down the roof, starting at the inside of each peak or valley.
2. When the rain reaches the edge of the roof, it will drip down.
3. When the rain meets another flow from above, the rain stops, and a cycle is completed.
4. When starting at a peak, the flow stops when it encounters a peak with greater magnitude. The same applies when it encounters a trough with a greater magnitude than the trough from which it started.

The counting method is illustrated in 3.10.

After counting the cycles, the total fatigue damage is calculated by comparing the number of cycles in the stress range, n_i, to the number of cycles to fail-

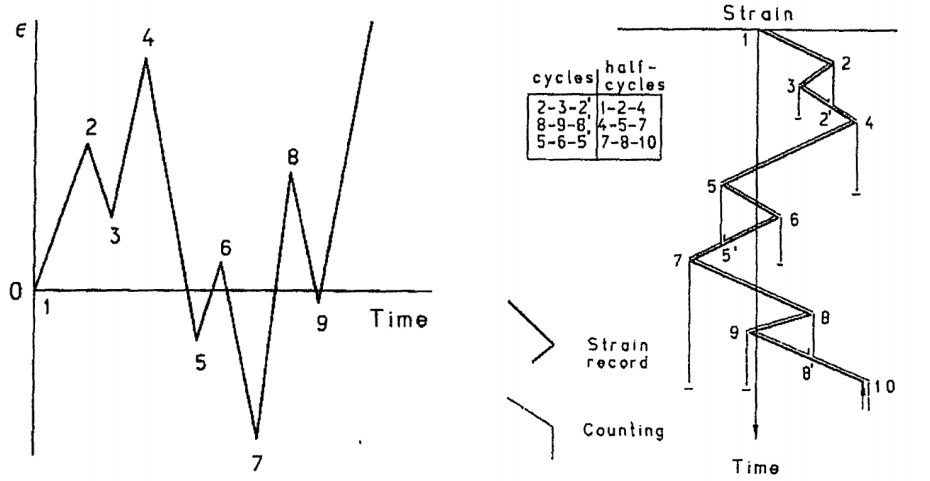

(a) Time history of a variable amplitude load

(b) Pagoda roof analogy of rainflow counting

Fig. 3.10: Illustration of the relationship between the time history and rainflow counting (Berge, 2006)

ure, N_i for stress range i. To get the total fatigue damage, the damage from each stress range is summed up in Equation (3.10). A total damage of $D = 1$ is defined as failure.

$$D = \sum_i \frac{n_i}{N_i} \leq 1 \tag{3.10}$$

3.4 Structural Dynamics

The blades and tower in FAST are modeled as Euler-Bernoulli beams. When using Euler-Bernoulli beams, small deflections of the beam are assumed. The deflection along the beam, $w(x)$, may then be calculated from the load applied, $q(x)$, where x is the length along the beam.

$$EI\frac{\mathrm{d}^4 w}{\mathrm{d}x^4} = q(x) \tag{3.11}$$

Here, E is the elastic modulus of the beam, and I is the second moment of area of the cross section of the beam. From the deflections, the moment,M, and shear force, M, in the beam may be calculated by:

$$M = -EI\frac{\mathrm{d}^2 w}{\mathrm{d}x^2} \tag{3.12}$$

$$Q = -EI\frac{\mathrm{d}^3 w}{\mathrm{d}x^3} \tag{3.13}$$

The shape of the deflection depends on the boundary conditions and on the loading. As the expression in Equation 3.11 contains a fourth order derivative, four boundary conditions must be applied to be able to calculate the deflection. Assuming no loads (free vibration), several displacement solutions, called mode shapes, may be calculated, along with the corresponding eigenfrequencies. Each of these mode shapes may be expressed as:

$$y = c_1 x + c_2 x^2 + c_3 x^3 + c_4 x^4 + c_5 x^5 + c_6 x^6 \tag{3.14}$$

where the coefficients for the mode shapes of the tower and blades, were calculated in Jonkman et al. (2009).

The motions of the beams are modeled using modal superposition, where the total deflection is expressed by superposing the deflections for all modes.

3.5 Time Integration

When simulating in the time domain, there are many methods of time integration to choose from. FAST uses a multistep fourth order Adams-Bashforth-Adams-Moulton predictor-corrector method (ABAM) with fixed time steps, initialized by 4th order Runge-Kutta integration over the first few steps.

The main difference between multistep methods such as ABAM, and one-step methods, is accuracy. One-step methods use information at a time step to

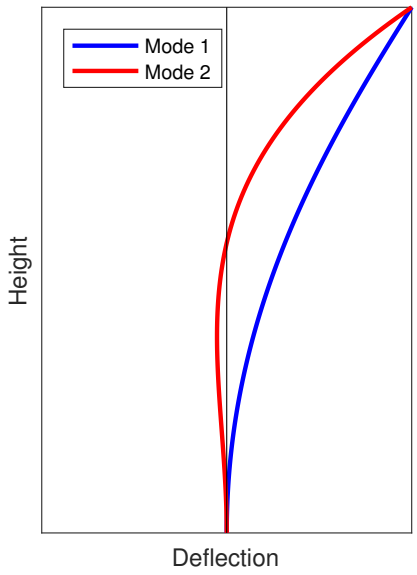

Fig. 3.11: Illustration of tower modes

predict dependent variables at the next time step, and then discard the information from the previous steps. Multistep methods instead retains the information, and uses this information to predict the next step more accurately.

The accuracy obtained by the extra information comes at the cost of extra computational time. As there are more steps to compute, the calculations take sligthly more time.

4. LONG TERM ENVIRONMENTAL CONDITIONS

4.1 Joint Long Term Distribution of wind and waves

The weather data for the site, provided by NKUA, contained measurements of wind and waves, for one hour periods over 10 years.

The long term environmental data is characterized by a joint distribution (Equation 4.1) of the significant wave height (H_s), spectral peak period (T_p), the wind speed 10m above MSL (U_w), and the misalignment between wind and wave directions (θ).

$$\begin{aligned} f_{\theta,U_w,H_s,T_p}(\theta,u,h,t) = f_\theta(\theta)\cdot f_{U_w|\theta}(u|\theta)\cdot f_{H_s|\theta,U_w}(h|\theta,u) \\ \cdot f_{T_p|\theta,U_w,H_s}(t|\theta,u,h) \end{aligned} \tag{4.1}$$

The H_s in the raw data showed little dependence on the misalignment angle θ, so it is assumed in this thesis that the conditional distribution $f_{H_s|\theta U_w}(h|\theta,u)$ may be simplified to only depend on the wind speed, $f_{H_s|U_w}(h|u)$. Likewise, the peak periods are a The joint distribution was herefore xpressed as:

$$f_{\theta,U_w,H_s,T_p}(\theta,u,h,t) \approx f_\theta(\theta)\cdot f_{U_w|\theta}(u|\theta)\cdot f_{H_s|U_w}(h|u)\cdot f_{T_p|H_s}(t|h) \tag{4.2}$$

The different parts of the joint probability distribution above are examined in the following sections.

4.2 Misalignment of Wind and Waves

To give an indication of the directionality of the wind and the waves, wind and wave roses were created for the waves and the wind speed at 10m above MSL. The wind rose in Figure 4.1 shows the relative frequency of the wind directions, while Figure 4.2 shows the mean wave directions. The directions are shown corresponding to a compass, meaning that 0° corresponds to wind and waves coming *from* East, 90° from North, 180° from West, and 270° corresponds to wind and waves from South.

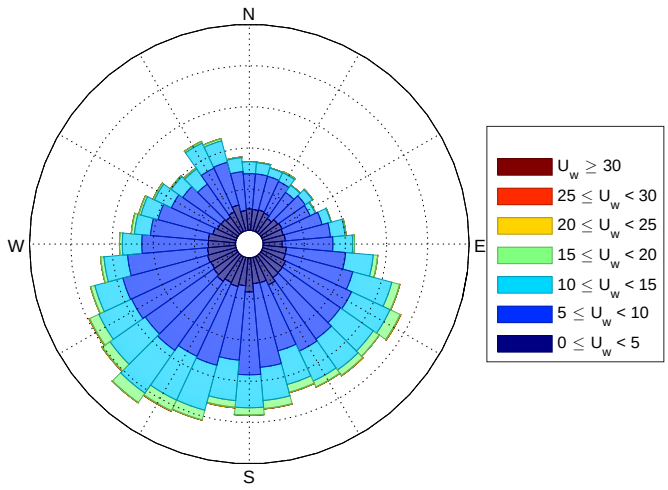

Fig. 4.1: Wind Rose

From the roses, it seems that the dominating wind direction does not coincide with the dominating direction of waves. While wave directions are mainly concentrated between 60° and 90°, the wind directions are more spread out. However, a closer examination of the relative angle between the wind and the wave, θ, the correlation is more apparent.

From the raw data, the absolute values of the relative misalignments between the wind and wave directions were calculated. Figure 4.3 shows the dis-

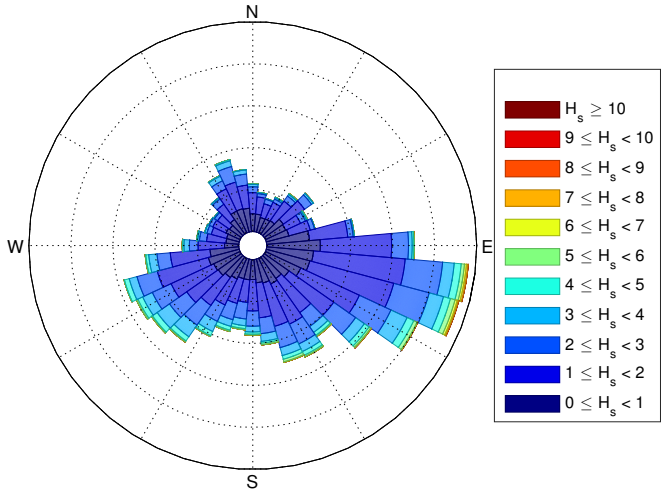

Fig. 4.2: Wave Direction Rose

tribution of the misalignment angles over 180°.

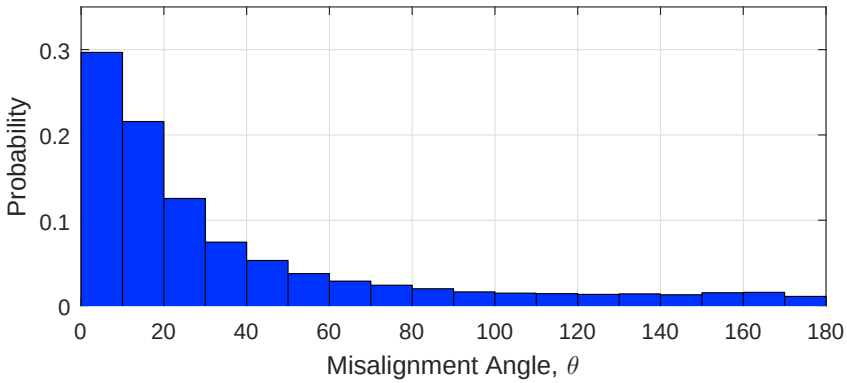

Fig. 4.3: Distribution of Misalignment Angles in Raw Data

The misalignment angles were divided into bins with width corresponding to the distribution in Figure 4.3. For small θ, the bin width was small, with the width increasing towards 180°, as shown in Figure 4.4. The probability of occurrence for each of these bins was calculated, and assigned to approximately the center of each bin, indicated by the blue lines in Figure 4.4.

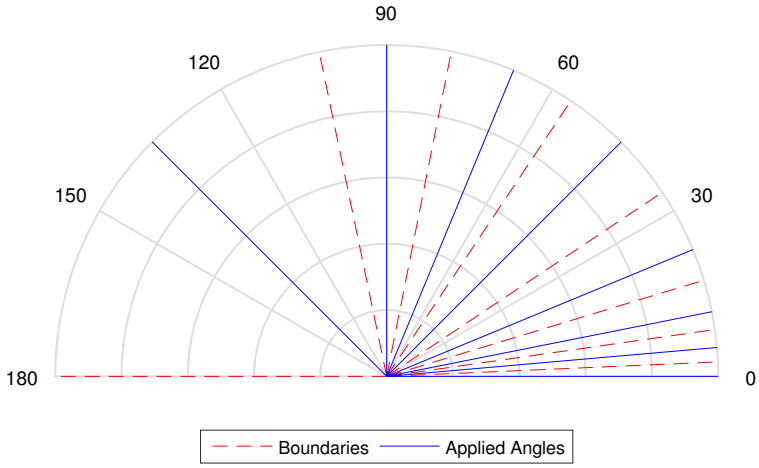

Fig. 4.4: Bins of Misalignment Angles

Tab. 4.1: Misalignment bins with corresponding probability of occurrence

Misalignment Angle, θ	Probability of Occurrence [%]
0.00°	10.662
5.00°	8.032
11.25°	16.484
22.50°	21.107
45.00°	21.313
67.50°	12.008
90.00°	6.314
135.00°	4.080
Sum	100.000

4.3 Wind Speeds

The one hour mean wind speeds at 10m height, U_w, seem to follow a two parameter Weibull distribution in each class of misalignment angles. The PDF of the marginal distribution is given in Equation (4.3).

$$f_{U_w|\theta}(u|\theta) = \frac{\alpha_U}{\beta_U}\left(\frac{u}{\beta_U}\right)^{\alpha_U - 1} \exp\left[-\left(\frac{u}{\beta_U}\right)^{\alpha_U}\right] \tag{4.3}$$

Here, the shape and scale parameters, α_U and β_U, are given by the misalignment. For each of the misalignment bins, the corresponding wind speeds were fitted to the distribution, with the parameters estimated by the Maximum Likelihood Method.

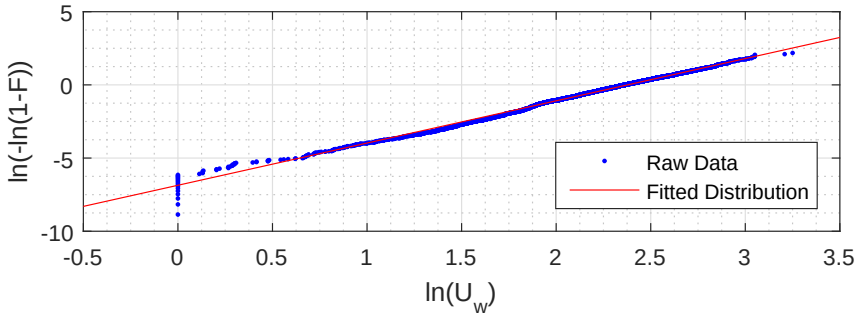

(a) $\theta = 0.0°$

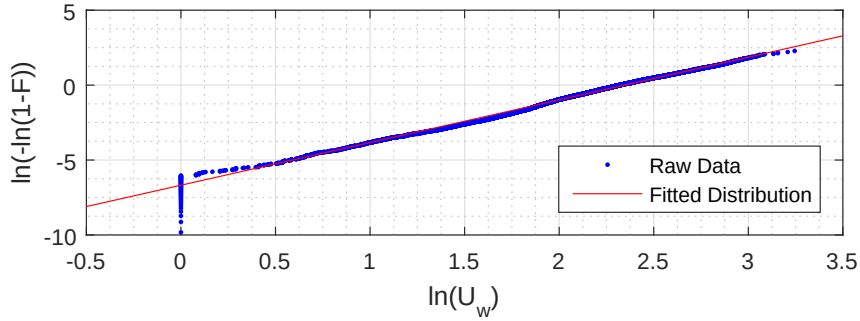

(b) $\theta = 11.25°$

Fig. 4.5: Conditional Distributions of U_w given θ

Figure 4.5 show the fitting of the raw data for two bins. The data is seen to fit well to the two parameter Weibull distribution. Note that the vertical line at $\ln U_w = 0 \Rightarrow U_w = 1$ is a result of the measurements not registering the wind speeds below 1m/s.

4.4 Significant Wave Heights

To calculate the parameters for the significant wave heights, the wind speeds were divided into bins of width 1m/s. For each of these bins, the corresponding significant wave heights, H_s seemed to follow a LoNoWe-distribution (Haver, 1980), a hybrid model containing the lognormal and the weibull distribution, with a shifting point, h_0, as shown in Equation 4.4.

$$f_{H_s}(h) = \begin{cases} \dfrac{1}{\sqrt{2\pi}\sigma h} \exp\left\{-\dfrac{1}{2}\left(\dfrac{\ln(h)-\mu}{\sigma}\right)^2\right\} & h \le h_0 \\ \dfrac{\alpha}{\beta}\left(\dfrac{h}{\beta}\right)^{\alpha-1} \exp\left\{-\left(\dfrac{h}{\beta}\right)^{\alpha}\right\} & h > h_0 \end{cases} \tag{4.4}$$

To simplify the conditionality between U_w and H_s, only the Weibull distribution was used:

$$f_{H_s|U_w}(h|u) = \frac{\alpha_H}{\beta_H}\left(\frac{h}{\beta_H}\right)^{\alpha_H-1} \exp\left[-\left(\frac{h}{\beta_H}\right)^{\alpha_H}\right] \tag{4.5}$$

The shape and scale parameters, α_H and β_H, were calculated for each of the bins. The parameters from each bin were fitted to the functions below, using the least squares method.

$$\alpha_H = a_1 + a_2 u^{a_3} \tag{4.6}$$

$$\beta_H = b_1 + b_2 u^{b_3} \tag{4.7}$$

The parameter for each bin, as well as the fitted function are shown in Figure 4.6, while the parameters for the fitted functions are listed in Table A.2.

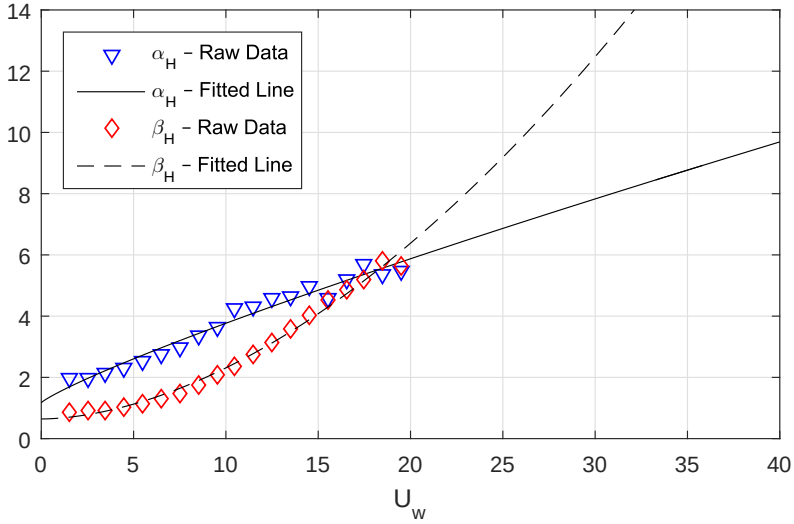

Fig. 4.6: Shape and Scale parameters for H_s given U_w

The distribution of H_s is shown in Figure 4.7 for two of the bins.

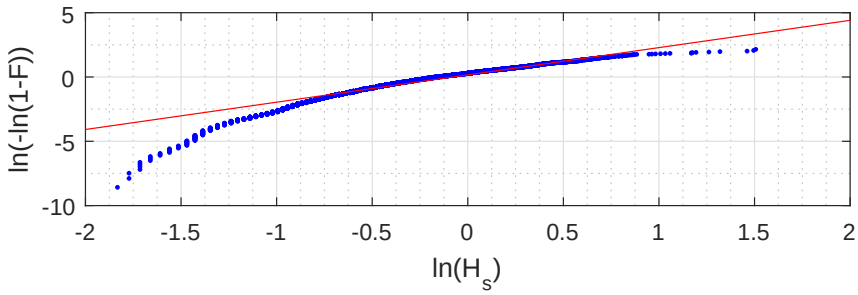

(a) $3m/s < U_w \leq 4m/s$

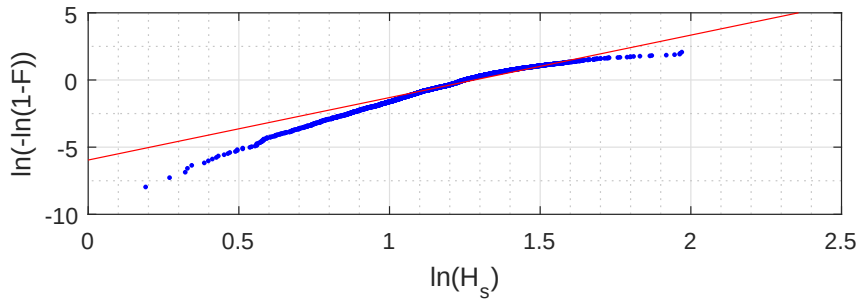

(b) $13m/s < U_w \leq 14m/s$

Fig. 4.7: Conditional Distributions of H_s given U_w

4.5 Peak Periods

The conditional distribution of the 1 hour peak periods, T_p, were estimated for different H_s. The wave heights were divided into bins with width of 0.5m, and the T_p in each class seemed to fit to a lognormal distribution, Equation (4.8).

$$f_{T_p|H_s}(t|h) = \frac{1}{\sqrt{2\pi}\sigma_T t} \exp\left\{-\frac{1}{2}\left(\frac{\ln(t)-\mu_T}{\sigma_T}\right)^2\right\} \tag{4.8}$$

As with the wave height distribution, the lognormal distribution parameters were fitted to smooth functions to describe the conditionality:

$$\mu_T = c_1 + c_2 u^{c_3} \tag{4.9}$$

$$\sigma_T^2 = d_1 + d_2 e^{d_3 h} \tag{4.10}$$

The estimated parameters from each bin are shown in Figure 4.8, along with the fitted function. The parameters describing the relationship between Hs and T_p and between U_w and H_s, are shown in Table A.2.

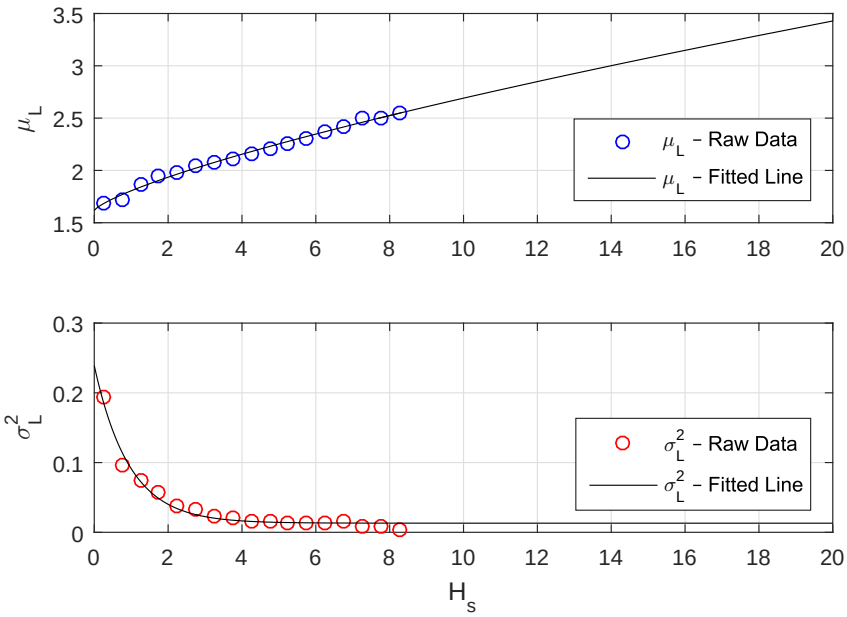

Fig. 4.8: Mean and Variance of Conditional Distribution of T_p given H_s

5. SHORT TERM ENVIRONMENTAL CONDITIONS

The raw data from NKUA describe the long term distribution of the wind and waves. In order to perform reliable dynamic analyses of the construction, the short term modeling of the environment must be considered. This chapter describes how the long term distributions of the hourly raw data were considered to model the short term distribution of the environment.

5.1 Wind

For time-domain response analysis, IEC-61400-1 (2005) suggests using a Kaimal spectrum to model the frequency contents of the turbulent wind field. This spectrum, shown in Equation 5.1, models the spectral density function for the three directions. Here, k represents the main longitudinal ($k = 1$), lateral ($k = 2$), and vertical ($k = 3$) directions.

$$S_k(f) = \sigma_k^2 \frac{\frac{4L_k}{U_{hub}}}{\left(1 + 6f\frac{L_k}{U_{hub}}\right)^{\frac{5}{3}}} \tag{5.1}$$

where f is the frequency (Hz), σ_k is the standard variation of the wind speed in the k direction, L_k is the integral length scale parameter. and U_{hub} is the wind speed at hub height. The parameters are given in Table 5.1, where the

longitudinal turbulence scale parameter, Λ_1, is given by the hub height, as:

$$\Lambda_1 = \begin{cases} 0.7 & \text{for } z_{hub} \leq 60m \\ 42 & \text{for } z_{hub} \geq 60m \end{cases} \tag{5.2}$$

For the NREL 5 MW turbine, which has a hub height of 90m, the longitudinal turbulence scale parameter is $\Lambda_1 = 42$.

Tab. 5.1: Distribution Parameters for U_w given θ

	Wind Speed Component Index, k		
	1	2	3
Standard Deviation, σ_k	σ_1	$0.8\sigma_1$	$0.5\sigma_1$
Integral Length Scale, L_k	$8.1\Lambda_1$	$2.7\Lambda_2$	$0.66\Lambda_1$

The wind speed in the longitudinal direction is represented by a mean value and a dynamic component, $U + u_1(t)$, while the lateral and vertical components are described by only the dynamic parts, $u_2(t)$ and $u_3(t)$. The dynamic components are zero-mean Gaussian distributed random processes, with standard deviation σ_k. For the Normal Turbulence Model (NTM), IEC-61400-1 (2005) suggests Equation 5.3 to get a representative value for the standard deviation in operational conditions.

$$\sigma_1 = I_{ref}\,(0.75U_{hub} + 5.6) = U_{hub}\,I \tag{5.3}$$

where I is the Turbulence Intensity factor, and $I_{ref} = 0.12$ is the reference value at a wind speed of 15 m/s.

In addition to the turbulence, the wind speeds change over height. The Normal Wind Profile (NWP) model describe the average wind speed as a function of the height:

$$U(z) = U_{hub}\left(\frac{z}{z_{hub}}\right)^{\alpha} \tag{5.4}$$

where z_{hub} is the hub height. This is also known as the Power Law. A quick examination of the raw data indicated that an exponent $\alpha = 0.1$ could be applied.

Using theses parameters, the turbulent wind fields were created in TurbSim. The wind fields were made up of longitudinal planes for each time step, were each plane consisted of 32x32 points. Each point then contained the velocities in all three directions.

5.2 Waves

5.2.1 Wave Spectra

The short term wave conditions are characterized by wave spectra (JONSWAP) defined by the significant wave height and spectral peak period, H_s and T_p respectively.

The JONSWAP wave spectrum is defined as:

$$S(\omega) = \alpha g^2 \omega^{-5} \exp\left\{-\frac{5}{4}\left(\frac{\omega}{\omega_p}\right)^{-4}\right\} \gamma^{\exp\left\{-\frac{(\omega/\omega_p - 1)^2}{2\sigma^2}\right\}} \tag{5.5}$$

where the peak enhancement factor, γ, the spectral width parameter, σ, and the generalized Phillips' Constant, α, are defined in Equations (5.6), (5.7) and (5.8).

$$\gamma = \begin{cases} 5 & \text{for} \quad \frac{T_p}{\sqrt{H_s}} \leq 3.6 \\ \exp\left\{5.75 - 1.15\frac{T_p}{\sqrt{H_s}}\right\} & \text{for } 3.6 < \frac{T_p}{\sqrt{H_s}} \leq 5.0 \\ 1 & \text{for } 5.0 < \frac{T_p}{\sqrt{H_s}} \end{cases} \tag{5.6}$$

$$\sigma = \begin{cases} 0.07 & \text{for } \omega \leq \omega_p \\ 0.09 & \text{for } \omega > \omega_p \end{cases} \tag{5.7}$$

$$\alpha = 5\pi^4 \frac{H_s^2}{g^2 T_p^4}(1 - 0.287 \ln \gamma) \tag{5.8}$$

To avoid unphysical high frequency waves, the wave spectra in this thesis are cut off at $\omega_{max} = \sqrt{\frac{2g}{H_s}}$ (Stansberg, 1998). The spectra are then smoothed around ω_{max}. Figure 5.1 shows an example of a JONSWAP Wave Spectrum used in the analyses.

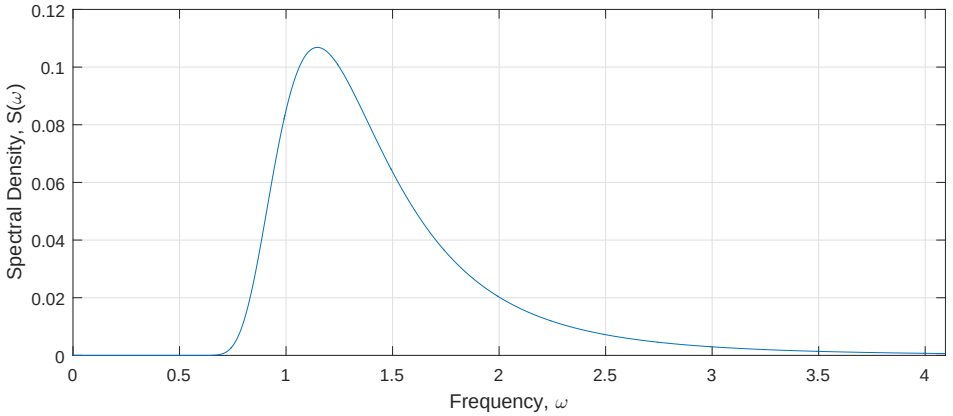

Fig. 5.1: JONSWAP Wave Spectrum for $H_s = 1.17m$, $T_p = 5.48s$

6. LOAD CASES

In order to ensure a conservative representation of the lifetime of a wind turbine, a range of load cases must be analysed. These load cases represent different combinations of wind and waves. As it is very time consuming to simulate all combinations, a range of representative load cases were chosen, using the raw data from NKUA.

Wind Speed

To adequately capture all load contributions from the wind, the wind speed range was chosen to include wind speeds between 1 m/s and 25 m/s. This corresponds to wind speed below cut-in, to model the idling turbine, going in steps of 1 m/s up to cut-out speed.

Significant Wave Height

From the probability distributions calculated for significant wave height given wind speed, Equation 4.5, the expected H_s was calculated for each U_w by:

$$H_s = E[H_s|U_w] = \beta_H \, \Gamma(\frac{1}{\alpha_H} + 1) \tag{6.1}$$

where α_H and β_H are the shape and scale parameters of the distribution, given by the wind speed bu Equations 4.6 and 4.7. The relationship between U_w and H_s is shown in Figure 6.1.

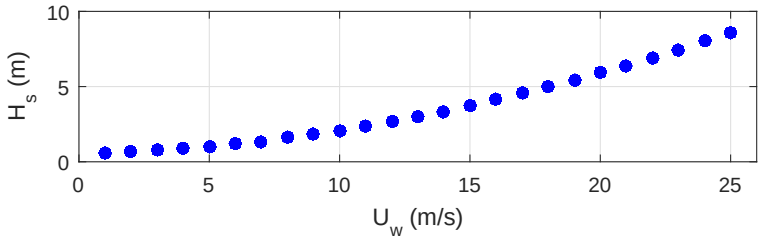

Fig. 6.1: Relationship between U_w and H_s for all loadcases

Peak Periods

The peak periods, T_p, of the load cases were chosen in a similar matter. From the distribution of T_p given H_s, Equation 4.8, the peak periods were calculated as:

$$Tp = E\left[T_p|H_s\right] = \exp\left(\mu_T + \frac{\sigma_T^2}{2}\right) \tag{6.2}$$

where μ_T and σ_T^2 were given by Equations 4.9 and 4.10. In addition, a set of T_p slightly above, and slightly below the expected value were chosen, as shown in Figure 6.2. This was done to examine the effect of the wave frequencies on the loads.

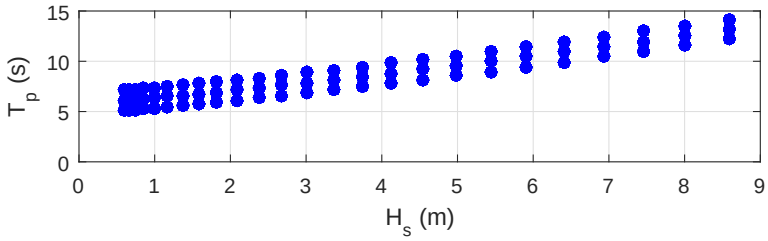

Fig. 6.2: Relationship between H_s and T_p for all loadcases

Given wind speeds of $U_w = 11$m/s and $U_w = 20$m/s, comparisons were made to see how the chosen load cases corresponded to the probability of occurrence in the raw data. Figure 6.3 show that the load cases chosen are representative.

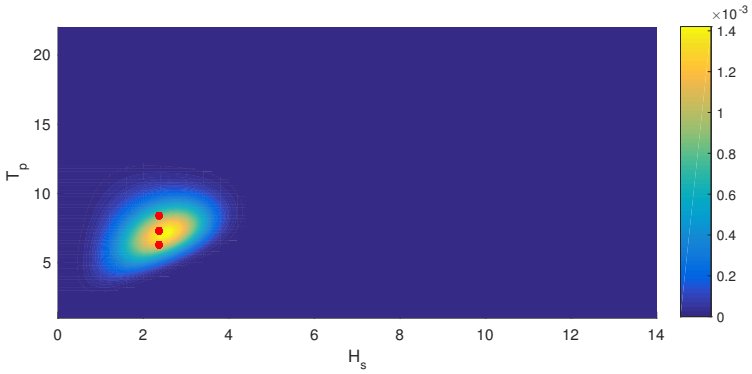

(a) $U_w = 11 m/s$

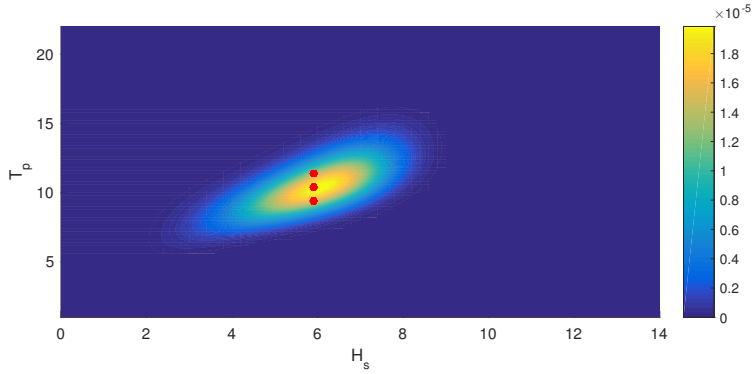

(b) $U_w = 20 m/s$

Fig. 6.3: Conditional Distributions of H_s given U_w

Relative Misalignment Between Wind and Waves

For an offshore wind turbine, the largest damping will be the aerodynamic damping, in the direction of the wind. This means that for waves coming from an angle of 90°, the wind turbine will experience no aerodynamic damping in the direction of the waves. The effects of the waves may therefore be larger, and potentially increase the fatigue damage. For this reason, the variation of wind and wave misalignment must also be taken into account when designing the load cases. As shown in Figure 4.3, the misalignment angles in the raw data were mainly close to 0°, and quickly decreased for increasing angles. Since most of

the misalignment angles are below 90° (see Table 4.1), and misalignment above 90° is assumed to contribute very little to fatigue, the misalignment angles were chosen between 0° and 90°.

7. POST-PROCESSING OF DATA

7.1 Calculation of Stress

In order to calculate fatigue damage, the results from FAST had to be processed in MATLAB. Since FAST models the wind turbine as beam elements, the dynamic response analyses resulted in time histories of the loads at the centerline of the tower, such as the axial force, N_x, or the side-to-side and fore-aft moments, M_x and M_y. The loads were output at 11 positions along the tower, with steps of 2.5m between the bottom ($z = -20m$) and $5m$ above the MSL. MATLAB was then used to calculate time series of the stress, by:

$$\sigma = \frac{N_z}{A} + \frac{M_y}{I} r \sin(\varphi) + \frac{M_x}{I} r \cos(\varphi) \tag{7.1}$$

where A is the cross sectional area, r is the outer radius of the tower, φ is the position and I is the second moment of area of the cross section. In order to get find the stress distribution around the tower, the stress histories were calculated for 8 positions around the perimeter of the tower, with steps of 22.5° (see Figure 7.1).

To minimize the transients in the beginning of the simulations, the turbine did not begin the analyses stationary. Instead, the initial conditions were modified, so the rotor speed and blade pitch matched the steady state conditions (see Figure 2.3). This meant that for each of the 10 minute simulations, a shorter initial startup period could be introduced. The simulations were therefore run for 650s, before the first 50s were removed. For all the environmental conditions,

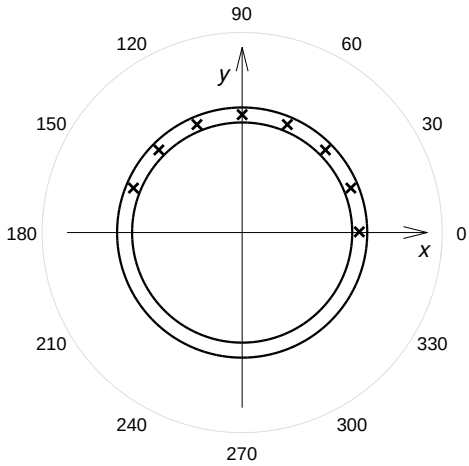

Fig. 7.1: Positions of Stress calculations relative to wind, U_w

analyses were run for three cases: Morison's Equation, MacCamy-Fuchs Theory, and with only wind, as shown in Figure 7.2.

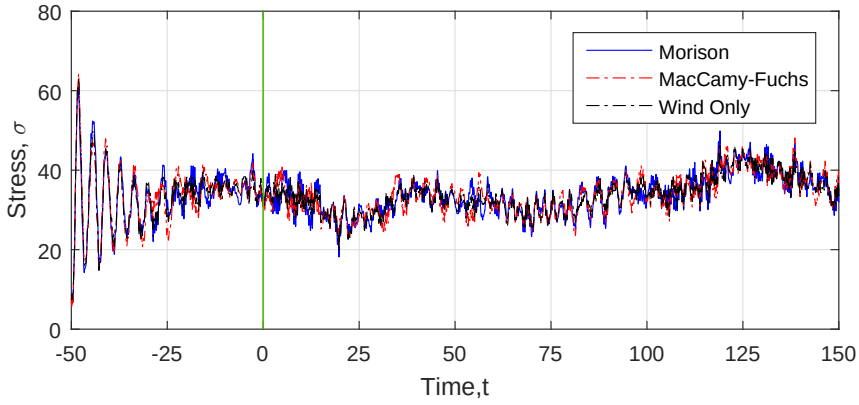

Fig. 7.2: Transient period in the beginning of the analyses

7.2 Fatigue Calculation

As described in Section 3.3, the fatigue calculation depends greatly on factors such as the environment. For the case of an offshore wind turbine, the environment is highly corrosive. To calculate the fatigue damage on the wind turbine,

Curve D in Figure 3.9 was therefore used with the parameters listed in Table 7.1. These results, corresponding to fatigue damage in seawater with cathodic protection, were calculated for each load case, and the results were scaled corresponding to the probability of occurrencee.

Tab. 7.1: Parameters for SN-curve

$N \leq 10^6$ cycles		$N > 10^6$ cycles		Fatigue limit at 10^7 cycles [MPa]	Thickness exponent	Reference Thickness [m]
m_1	$\log a_1$	m_2	$\log a_2$	σ_{lim}	k	t_{ref}
3.0	11.764	5.0	15.606	52.63	0.2	0.032

The fatigue damage was calculated through rainflow counting, using the WAFO toolbox for MATLAB, developed by the WAFO-group (2011). The original script was made for single sloped SN curves, so a modified version was used to account for the two slopes in the applied curve.

When calculating the fatigue damage over 20 years, the damage from the 10 minute simulations were simply extrapolated to 20 years. The damage was then weighted, using the probabilities for each sea state.

7.3 Spectral Analysis

In order to investigate the responses of the wind turbine in the frequency domain, power spectra were calculated for the responses the WAFO toolbox. An investigation of these power spectra can reveal differences in the methods of modeling, and also indicate what kind of loads dominate. As with the time series, the spectral analyses were performed for the two hydrodynamic models, and with only wind. It should be noted that the calculated spectra are very sensitive to spectrum smoothing, meaning that the values may not be exact. However, as the same smoothing was used on all spectra, they may be used to compare the frequency response between the different methods and load cases.

A comparison between the power spectra for the stress at the is shown in Figure 7.3. The differences between Morison (M1), MacCamy-Fuchs (MF) and only wind (W) are negligible for the purely wind driven loads, such as around f_{3p} and for the low frequency wind turbulence (LF). However, the wave frequency (WF) loads show the differences more clearly.

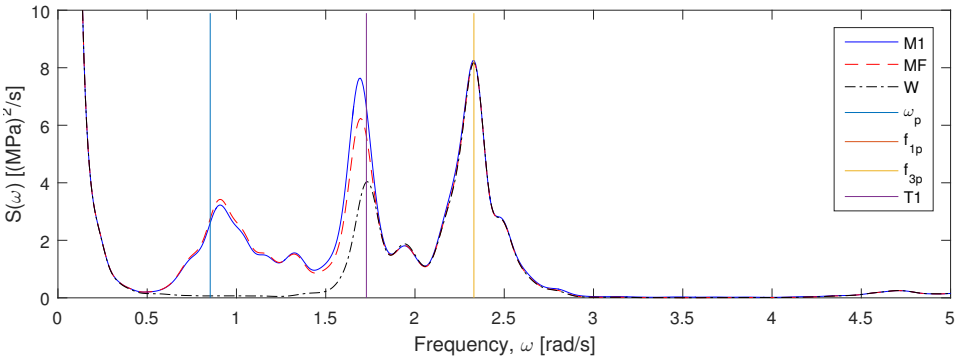

Fig. 7.3: Comparison of load spectra for stress at the bottom, $U_w = 5.0\text{m/s},\ H_s = 1.0\text{m},\ T_p = 7.37\text{s},\ \theta = 0.0°$

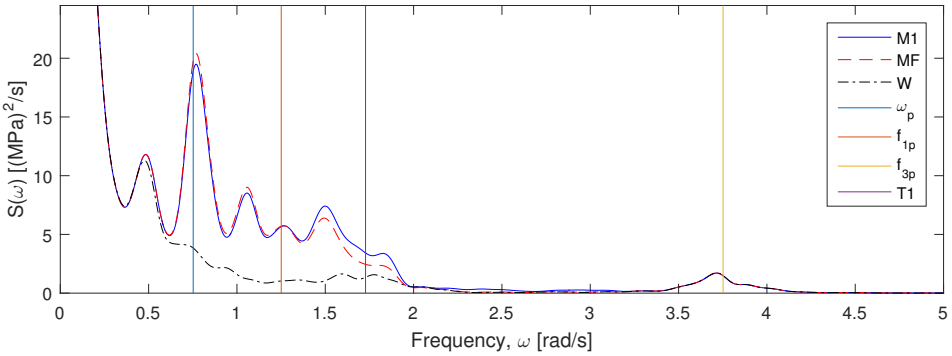

Fig. 7.4: Comparison of load spectra for stress at the bottom, $U_w = 11\text{m/s} H_s = 2.37\text{m} T_p = 8.35\text{s} \theta = 0.0°$

8. RESULTS AND DISCUSSION

Simulations have been performed on the wind turbine, in order to investigate the effect of hydrodynamic modeling. The simulations are investigated in this chapter.

8.1 Effect of Weather

In order to investigate the effect of the different weather conditions, a range of load cases were examined. The load cases in question are listed in Table 8.1.

The spectra in this section show the stress at the bottom of the structure, in the direction of the wind. The power spectra of the stress are marked as $S_{M1}(\omega)$ and $S_{MF}(\omega)$ for the spectra calculated with Morison's equation and with MacCamy-Fuchs, respectively. The power spectra of the wave elevation, $S_W(\omega)$, are included in the figures, to visualize where the frequencies that are affected by the waves.

The rotor frequency and the blade passing frequency are marked with f_{1p} and f_{3p}. These are approximate values, as they change with time. The frequencies shown are calculated using the mean rotor speed of the load case.

In addition, the first tower eigenfrequency and the peak frequency of the wave spectra are marked as $T1$ and T_p.

Tab. 8.1: Load cases for examination of weather effects

Load Case	Mean Wind Speed U_w [m/s]	Significant Wave Height H_s [m]	Spectral Peak Period T_p [s]
1a	1	0.60	7.12
1b	1	0.60	6.12
1c	1	0.60	5.12
2a	5	1.00	7.37
2b	5	1.00	6.37
2c	5	1.00	5.37
3a	11	2.37	8.35
3b	11	2.37	7.35
3c	11	2.37	6.35
4a	20	5.91	11.44
4b	20	5.91	10.44
4c	20	5.91	9.44

Load Case 1 - $U_w = 1\,m/s$

The response spectra of the fore-aft stress at the bottom for loadcases 1.1a, 1.1b and 1.1c are shown in Figure 8.1-8.2, comparing the spectra computed with Morison's equation to the spectra computed with MacCamy-Fuchs. As the wind loads are small, the differences from the wave excitation forces are very clear. The main peaks are at the frequencies corresponding to the first tower eigen-frequency, T1, and the blade passing frequency, f_{3p}. However, as the peak of the wave spectra, T_p, are close to T1, the high frequency waves excite the tower. As the mass terms are smaller for high frequency waves when using MacCamy-Fuchs, the forces are smaller, and the peaks are therefore lower than for Morison's equation.

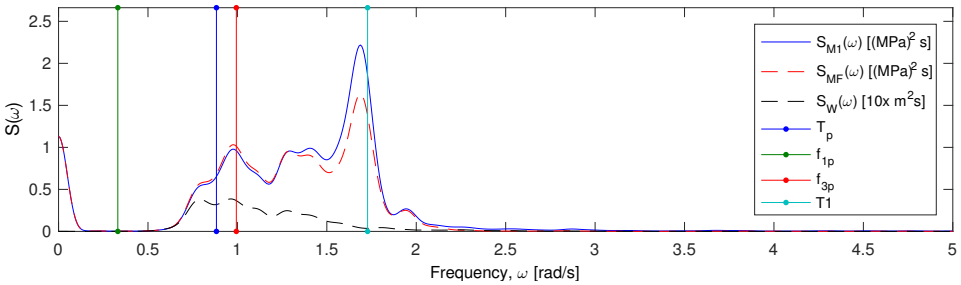

Fig. 8.1: Spectral density of the stress at the bottom - Load Case 1a

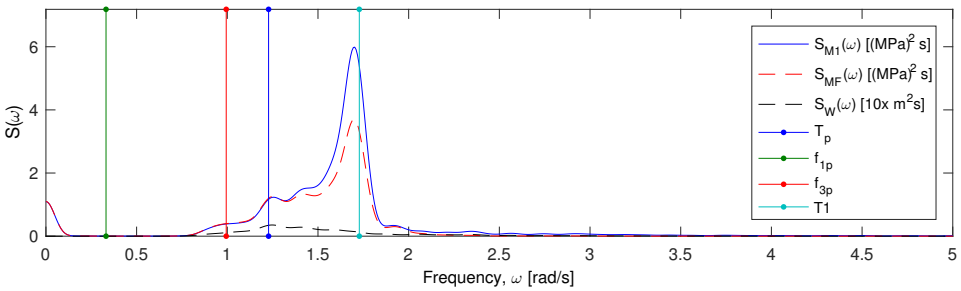

Fig. 8.2: Spectral density of the stress at the bottom - Load Case 1c

Load Case 2 - $U_w = 5m/s$

When the wind speed increases, the aerodynamic effects increase in importance. As the power spectrum of the stress in Figure 8.3 shows, there is a peak at approximately 2.4 rad/s, corresponding to f_{3p}. Note that the wave excitation in the high frequency range show a clear difference between M1 and MF, while the peaks excited by the wind are approximately equal. The low frequency excitation by the wind is equal for both M1 and MF. As the wind speed increases, the energy in the low end of the spectrum increases significantly. To be able to compare the higher frequency ranges, this low frequency part of the spectra are cut off.

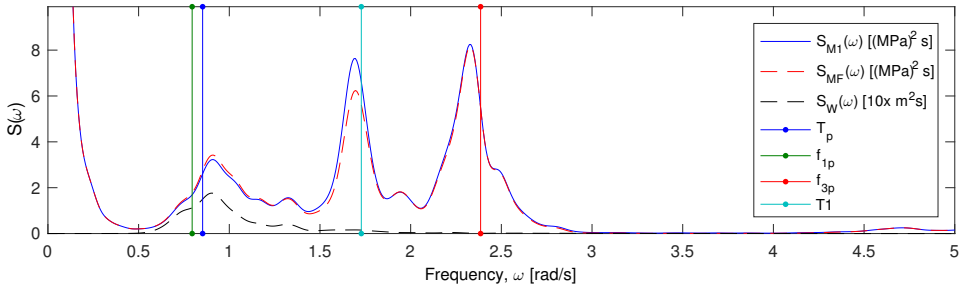

Fig. 8.3: Spectral density of the stress at the bottom - Load Case 2a

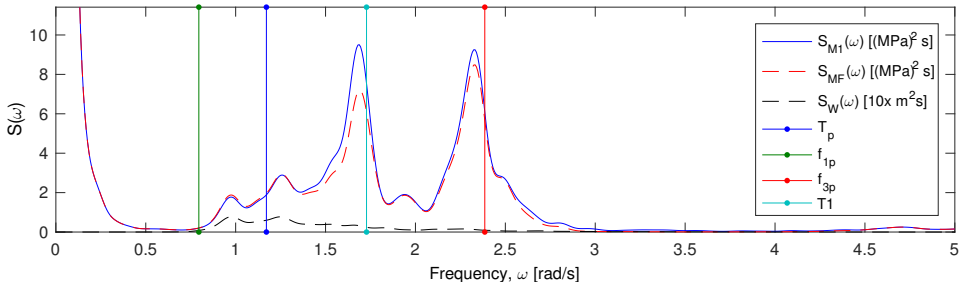

Fig. 8.4: Spectral density of the stress at the bottom - Load Case 2c

Load Case 3 - $U_w = 11 m/s$

The spectra in Figures 8.5-8.6 show that the blade passing frequency f_{3p} decreases in importance as the wind speed increases, due to aerodynamic damping. As f_{3p} move away from the wave frequencies, the peaks become equal for M1 and MF.

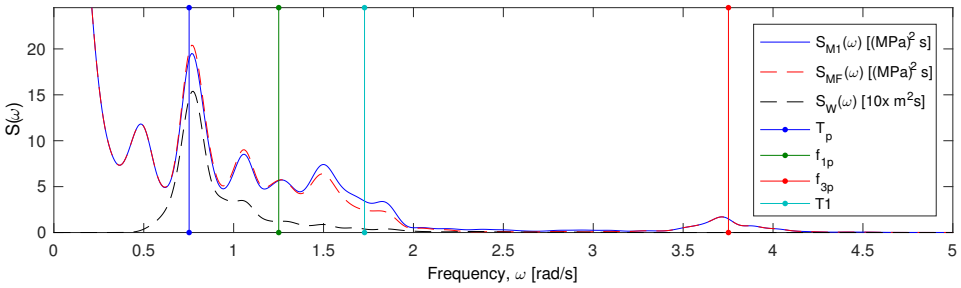

Fig. 8.5: Spectral density of the stress at the bottom - Load Case 3a

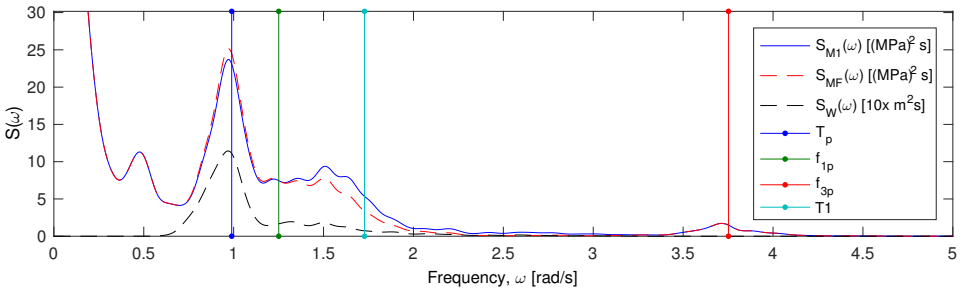

Fig. 8.6: Spectral density of the stress at the bottom - Load Case 3c

Load Case 4 - $U_w = 20 m/s$

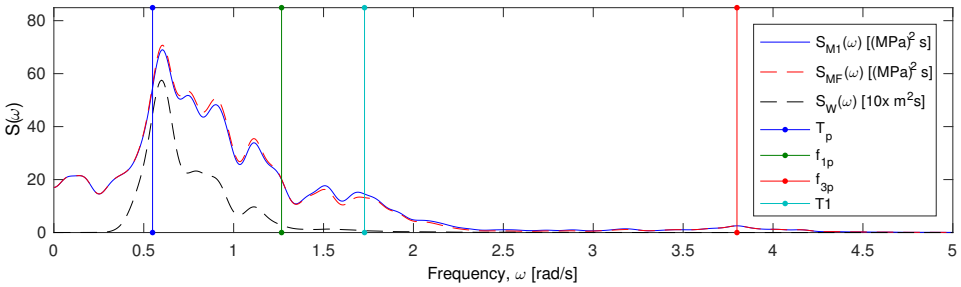

Fig. 8.7: Spectral density of the stress at the bottom - Load Case 4a

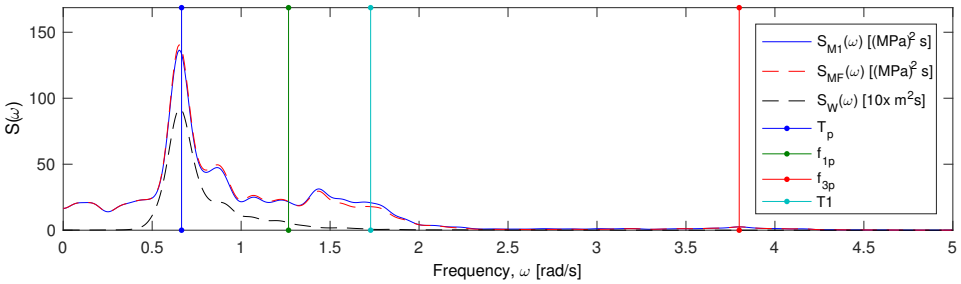

Fig. 8.8: Spectral density of the stress at the bottom - Load Case 4c

8.2 Damage on the tower

When combining the damage from all load cases, the difference between the fatigue lives could clearly be seen. Figure 8.9 shows the fatigue damage around the circumference of the tower at the mudline. The shape of the distribution is due to the fact that all wind always was in the same direction, 0°, and thus increasing the damage in the fore-aft direction. As could be expected from the load spectra, the damage at the bottom from MacCamy-Fuchs is slightly larger than the damage from using Morison's equation.

The difference in damage between the bottom at at the MSL is very large. As Figure 8.10 shows, the circumferential fatigue damage at the MSL is an order of magnitude smaller than at the bottom. However, the fatigue damage here is

Tab. 8.2: Mean and standard deviation of the time series of the stress at the bottom.

Load Case	Morison		MacCamy-Fuchs		Difference [%]	
	Mean [MPa]	STD [MPa]	Mean [MPa]	STD [MPa]	Mean	STD
1.1a	7.54	1.11	7.54	1.04	0	-6.31
1.1b	9.82	1.94	9.82	1.91	0	-1.55
1.1c	12.08	2.54	12.08	2.51	0	-1.18
1.2a	15.56	3.20	15.57	3.18	0.06	-0.63
1.2b	18.59	4.19	18.59	4.16	0	-0.72
1.2c	22.83	4.15	22.83	4.14	0	-0.24
1.3a	27.49	4.57	27.49	4.52	0	-1.09
1.3b	33.14	4.67	33.15	4.65	0.03	-0.43
1.3c	40.63	6.11	40.63	6.09	0	-0.33
1.4a	47.60	7.60	47.60	7.58	0	-0.26
1.4b	51.84	5.51	51.84	5.47	0	-0.73
1.4c	47.62	7.45	47.62	7.42	0	-0.40

different than the damage at the bottom, as the damage is larger when using Morison's equation.

The maximum fatigue damage at the bottom and at the MSL are compared for each seed in Tables 8.3 and 8.4, while the differences are shown in Figure 8.11.

Tab. 8.3: Maximum fatigue damage at the bottom

Seed	Morison	MacCamy-Fuchs	Difference (%)
1	2.595	2.656	3.13
2	2.44	2.516	2.24
3	2.552	2.609	2.14
4	3.151	3.218	3.80
5	2.513	2.608	3.06
6	2.485	2.561	2.37
Mean	2.623	2.695	2.79

A distribution of the maximum fatigue damage for one of the seeds is shown in Figure 8.12, where it is clearly seen that the differences increase with increasing depth. Note that the differences above MSL are approximately constant.

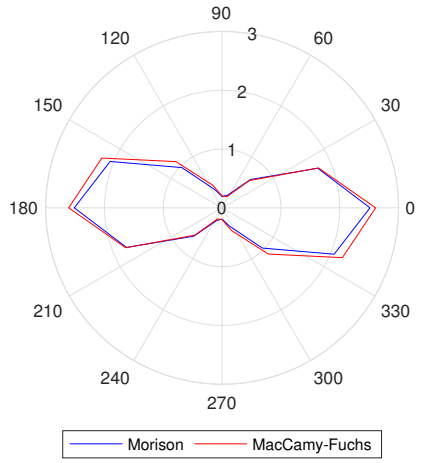

Fig. 8.9: Maximum Fatigue damage at the mudline

Tab. 8.4: Maximum fatigue damage at MSL

Seed	Morison	MacCamy-Fuchs	Difference (%)
1	0.303	0.295	-2.92
2	0.279	0.271	-2.52
3	0.293	0.286	-2.51
4	0.390	0.380	-2.63
5	0.283	0.275	-2.19
6	0.298	0.291	-2.76
Mean	0.308	0.300	-2.59

This is because there is no wave excitation above MSL, as wave stretching is not included.

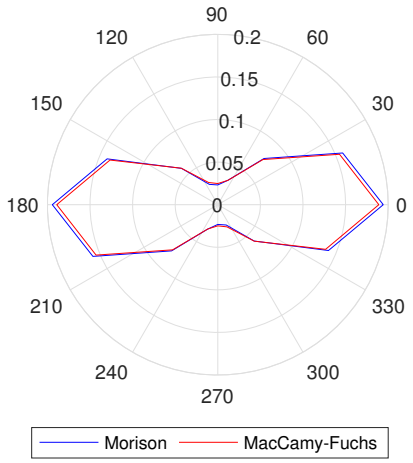

Fig. 8.10: Maximum Fatigue damage at MSL

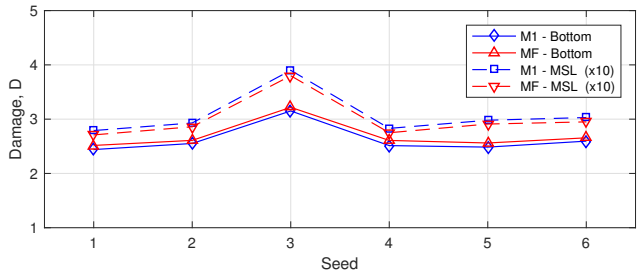

Fig. 8.11: Maximum damage at bottom - Comparison of seeds

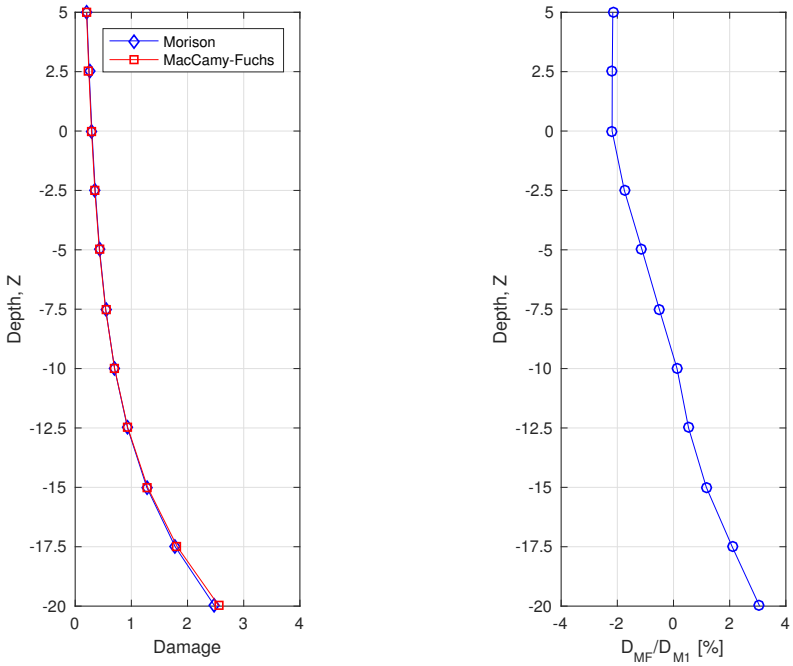

(a) Maximum Fatigue damage *(b)* Fatigue damage difference

Fig. 8.12: Distribution of maximum fatigue damage along the length of the tower

8.3 Fatigue Contributions

The damage at the bottom was sorted to investigate which load cases contributed the most to fatigue damage. As Table 8.5 shows, there is a clear trend. All the load cases with the most damage have a wind speed around rated wind speed (11.4 m/s), while the misalignment angles that contribute the most are 11.25° and 22.5°. This suggests that although there are differences between the hydrodynamic models, the aerodynamics are much more important. As shown in Figure 2.3, the thrust is largest around rated wind speed, leading to more fatigue damage. In addition, misalignments of 11.25° and 22.5° result in the least aerodynamic damping, which also contribute significantly to the fatigue damage.

Tab. 8.5: Load cases with the most fatigue damage

Rank	U_w	H_s	T_p	θ
1	12	2.6826	7.5956	11.25
2	14	3.3653	8.1541	11.25
3	13	3.0132	7.8628	11.25
4	12	2.6826	6.5956	11.25
5	12	2.6826	6.5956	22.5
6	13	3.0132	6.8628	11.25
7	14	3.3653	7.1541	11.25
8	12	2.6826	7.5956	22.5
9	12	2.6826	8.5956	11.25
10	16	4.1327	8.8108	11.25
11	15	3.7385	8.4699	11.25
12	14	3.3653	7.1541	22.5
13	13	3.0132	8.8628	11.25
14	9	1.8229	5.935	11.25
15	12	2.6826	7.5956	0
16	13	3.0132	6.8628	22.5
17	14	3.3653	9.1541	11.25
18	12	2.6826	6.5956	0
19	12	2.6826	8.5956	22.5
20	13	3.0132	7.8628	22.5

9. SUMMARY AND RECOMMENDATIONS

In this thesis, an investigation has been performed on how hydrodynamic loading effects influence the fatigue life of an offshore wind turbine. A code was developed to run FAST with MacCamy-Fuchs theory instead of the standard Morison's equation. Hindcast data from the North Sea was the used to simulate the weather over 20 years, to investigate the responses and fatigue damage of the wind turbine.

The results in Chapter 8 show that there are small differences between the loads with Morison's equation and the loads with MacCamy-Fuchs theory. While the mean forces are approximately the same using either of the models, there are small differences when the dynamic effects are taken into account. Table 8.2 shows that there is no difference in the mean stress at the bottom for the two hydrodynamic models. There are, however, small differences in the standard deviations. These differences are mostly noticable for the small waves.

When looking at the fatigue damage on the tower, a clear difference can be seen. At the bottom, where the stresses are largest, MacCamy-Fuchs theory leads to slightly more damage than Morison's equation. This is due to the fact that the inertia coefficients for the large waves are slightly larger for MacCamy-Fuchs . As the large waves decay slowly towards the bottom, the difference is clear in the fatigue damage.

The fatigue damage at the MSL is slightly lower for MacCamy-Fuchs than for Morison. This because Morison's equation overestimates the forces from short waves. As the short waves decay fast towards the bottom, the effect of this is

most apparent at the MSL.

Although there are differences between the hydrodynamic models, the structure analysed in this thesis does not seem very sensitive to this. In addition, the maximum contribution to the fatigue damage came from load cases with large thrust from the wind, suggesting that aerodynamics may be more important with respect to fatigue damage.

9.1 Further work

There are several improvements that can be done to further investigate the results in this thesis. First, a study should be performed to investigate the effect of the wind direction. In this thesis, the wind direction was constant, leading to significantly more fatigue at some places around the perimeter. By analysing the wind turbine with different wind directions, a better comparison between MacCamy-Fuchs and Morison may be performed.

In addition to the wind directions, a study should be performed on different diameters of the structure. As larger cylinder will experience more diffraction, this may give a better understanding of the differences between the hydrodynamic theories, and how they affect large wind turbines.

An investigation should also be performed on a hybrid model between Morison's equation and MacCamy-Fuchs theory. While there are differences between the models, they are most apparent for small waves. However, as the waves grow in size, diffraction becomes less important. In addition, the wave crests become more important when the waves are larger. Therefore, a fatigue analysis should be performed where MacCamy-Fuchs is used for small waves, where diffraction is important, and wave crests are not. For larger waves, the wave kinematics may be integrated to the wave crest, and the forces estimated using Morison's equation.

REFERENCES

Berge, S. (2006). Fatigue Design of Welded Structures.

DNV-RP-C203 (2011). Fatigue Design of Offshore Steel Structures. *Recomm. Pract.*

Faltinsen, O. M. (1990). *Sea Loads on Ships and Offshore Structures*. Cambridge University Press.

GWEC (2015). Global Wind Report: Annual Market Update 2015. *Glob. Wind Rep.*

Haver, S. (1980). *Analysis of Uncertainties Related to the Stochastic Modelling of Ocean Waves*. PhD thesis, Norwegian Institute of Technology, Trondheim, Norway.

IEC-61400-1 (2005). International Standard IEC-61400-1.

Jonkman, J. M. and Buhl, M. L. (2005). FAST User's Guide Updated August 2005.

Jonkman, J. M., Butterfield, S., Musial, W., and Scott, G. (2009). Definition of a 5-MW Reference Wind Turbine for Offshore System Development. *Tech. Rep.*

Jonkman, J. M. and Musial, W. (2010). Offshore Code Comparison Collaboration (OC3) for IEA Task 23 Offshore Wind Technology and Deployment. *Tech. Rep.*

Li, L., Gao, Z., and Moan, T. (2013). Joint Environmental Data At Five European Offshore Sites for Design of Combined Wind and Wave Energy Devices. *OMAE*.

MacCamy, R. C. and Fuchs, R. A. (1954). Wave Forces on Piles: A Diffraction Theory. *Beach Eros. Board Tech. Memo.*

Malik, M. (2015). Hydrodynamic Modeling of Forces on Vertical Cylinders. *Proj. Thesis.*

Moriarty, P. J. and Hansen, A. C. (2005). AeroDyn Theory Manual. *Renew. Energy.*

Stansberg, C. T. (1998). Second-order effects in random wave modeling. In *Int. Symp. Waves - Phys. Numer. Model.*, volume 2, pages 793–802.

WAFO-group (2011). {WAFO} - A Matlab Toolbox for Analysis of Random Waves and Loads - A Tutorial.

APPENDIX

A. STATISTICAL DISTRIBUTION PARAMETERS

Tab. A.1: Distribution Parameters for U_w given θ

Angle, θ	α_U	β_U
0.00	2.885	10.776
5.00	2.881	10.807
11.25	2.849	10.435
22.50	2.703	8.955
45.00	2.436	7.311
67.50	2.252	6.133
90.00	2.125	5.590
135.00	1.985	5.933

Tab. A.2: Parameters for Conditionality between Distributions

Distribution Parameter	Equation	Parameter	Value
α_H	(4.6)	a_1	1.1717
		a_2	0.3608
		a_3	0.8571
β_H	(4.7)	b_1	0.6420
		b_2	0.0275
		b_3	1.7827
μ_T	(4.9)	c_1	1.6157
		c_2	0.1895
		c_3	0.7537
σ_T^2	(4.10)	d_1	0.0131
		d_2	0.2258
		d_3	–1.0611

B. SCATTER DIAGRAM OF MISALIGNMENT AND WIND SPEED

Tab. B.1: Scatter diagram of wind speed and misalignment angle, given as percentages of total number of measurements.

$U_w \backslash \theta$	0-15	15-30	30-45	45-60	60-75	75-90	90-105	105-120	120-135	135-150	150-165	165-180	Sum
0-2	0.3845	0.3822	0.3206	0.3685	0.2921	0.3366	0.2191	0.2567	0.2191	0.2054	0.1632	0.1312	3.2792
2-4	1.6418	1.4946	1.2128	1.0896	0.9721	0.931	0.7313	0.7188	0.6207	0.5773	0.5123	0.3548	10.857
4-6	4.1313	3.2071	2.3606	1.7	1.2311	0.8876	0.7131	0.5591	0.607	0.6104	0.6731	0.4278	17.108
6-8	8.8855	6.0549	3.352	1.7456	0.9744	0.6172	0.4952	0.3617	0.413	0.3446	0.5579	0.3183	24.12
8-10	9.2963	4.8969	1.7331	0.818	0.4062	0.243	0.1472	0.1244	0.1027	0.1221	0.2259	0.2567	18.372
10-12	7.7229	3.1204	0.7678	0.2921	0.1449	0.0833	0.0559	0.0365	0.0365	0.0479	0.1209	0.1312	12.56
12-14	4.8432	1.7103	0.3457	0.1346	0.0491	0.0319	0.0103	0.0171	0.008	0.0251	0.0719	0.097	7.3442
14-16	2.9972	0.7222	0.1015	0.0411	0.008	0.0046	0.0057	0.0034	0.0011	0.0023	0.0262	0.0468	3.9601
16-18	1.3349	0.2248	0.0399	0.008	0.0011	0.0034	-	0.0023	0.0011	0.0011	0.0011	0.0091	1.6268
18-20	0.4997	0.089	0.024	0.0034	0.0011	-	-	-	-	-	-	-	0.6172
20-22	0.1084	0.0262	0.0023	-	-	-	-	-	-	-	-	-	0.1369
22-24	0.0046	0.0023	-	-	-	-	-	-	-	-	-	-	0.0069
24-26	0.0091	0.0011	-	-	-	-	-	-	-	-	-	-	0.0102
26-28	-	-	-	-	-	-	-	-	-	-	-	-	-
28-30	-	-	-	-	-	-	-	-	-	-	-	-	-
Sum	41.859	21.932	10.26	6.2009	4.0801	3.1386	2.3778	2.08	2.0092	1.9362	2.3525	1.7729	100